國 立 交 通 大 學

材 料 科 學 與 工 程 系
奈 米 科 技 研 究 所

碩 士 論 文

以新穎設計之錐形奈米陣列展現形貌調控、高穩定性、水潔淨及具方向異性之多功能類壁虎黏貼結構

A geometry-controllable, anisotropic, highly stable and water cleanable gecko-like adhesive via innovative design of taper nanohairs.

研 究 生 ： 丁懷箴　　　Huai-Chen Ting

指導教授 ： 柯富祥 教授　Prof. Fu-Hsiang Ko

中 華 民 國 九 十 九 年 八 月

以新穎設計之錐形奈米陣列展現形貌調控、高穩定性、水潔

淨及具方向異性之多功能類壁虎黏貼結構

A geometry-controllable, anisotropic, highly stable and water cleanable gecko-like adhesive via innovative design of taper nanohairs.

研 究 生：丁懷箴　　　　Student：Huai-Chen Ting

指導教授：柯富祥　　　　Advisor：Prof. Fu-Hsiang Ko

國 立 交 通 大 學

材 料 科 學 與 工 程 系 奈 米 科 技 研 究 所

碩 士 論 文

A Thesis

Submitted to Institute of Nanotechnology

Department of Materials Science and Engineering

College of Engineering

National Chiao Tung University

in partial Fulfillment of the Requirements

for the Degree of

Master

in

Nanotechnology

August 2010

Hsinchu, Taiwan, Republic of China

中華民國九十九年八月

Acknowledgment

i

# 以新穎設計之錐形奈米陣列展現形貌調控、高穩定性、水潔淨及具方向異性之多功能類壁虎黏貼結構

研究生:丁懷箴　　　　　　　　　　　指導教授:柯富祥 教授

國立交通大學材料科學與工程系奈米科技研究所 碩士班

摘 要

　　由壁虎腳所引起的乾式黏附力已引起了各界的關注,透過表面的粗糙度和指向性的改變,使其擁有強大的黏附力和微弱的脫附力且可重複使用為其迷人之處。近來,關於壁虎腳的仿生結構在理論及實驗方面的研究已被相繼提出。然而,這些研究與自然的壁虎相比之下,有著受限於材料方面的缺點;但在我們的研究中, 我們設計了一有效的方法來製作出創新的結構來更符合理想的乾式吸附力。我們首次提出,以去耦兩階段硬式陽極氧化的方式,來製作出長1.3微米、直徑380奈米的錐形陽極氧化鋁模板;經過翻模的過程後,得到了具有傾斜角度的錐狀奈米陣列。此錐狀奈米陣列在大面積的表現上具備了出色的方向性、可重複使用性及水潔淨的特性。與一般的柱狀奈米陣列相比,錐狀奈米陣列有更好的穩定性和自潔淨的特性。藉由錐狀奈米陣列在各具方向性的力上亦有出色的表現:剪力可達到每平方公分8牛頓之強, 而反方向的脫附力卻僅需要每平方公分1.4牛頓。在未來, 此優越的黏附力可被應用於爬行機器人、液晶螢幕工廠無污染搬運系統、以及無殘留的貼紙。我們堅信, 此新穎的結構,由於其便宜的造價,

整合了出色的黏附力，加之具高度穩定性和自潔淨等優點，在新的世代裡將會

被佔有一席之地！
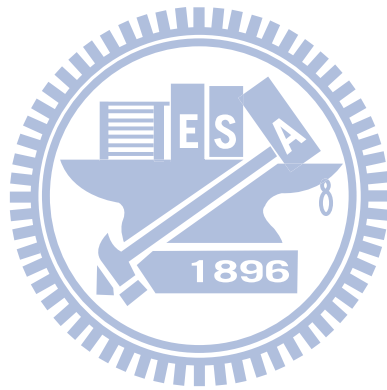
A geometry-controllable, anisotropic, highly stable and water cleanable gecko-like adhesive via innovative design of taper nanohairs.

Student : Huai-Chen Ting   Advisor : Prof. Fu-Hsiang Ko

Department of Materials Science and Engineering
Institute of Nanotechnology
National Chiao Tung University

Abstract

Dry adhesion inspired by gecko's feet has attracted much attention because it provides strong, yet reversible attachment against surfaces of varying roughness and orientation. Recently, theoretical and experimental investigations into the field of mimicking gecko adhesives have reported; however, they suffered from some disadvantages due to materials' limitation compared with nature material from gecko. In this study, we designed the efficient method of an innovate structure for ideal dry adhesives. A taper anodic alumina oxide mold with a length of 1.3 μm and a diameter of 380 nm was fabricated using decoupling two-step hard-anodization process which was firstly reported by us. After molding, taper-shaped nanohair array with slanted angle was presented. The approach to fabricate angled taper nanohair arrays obtained an excellent directional, reusable, and water cleanable use in large area. The angled taper nanohair facilitated the stability and self-cleaning properties compared with pillar nanohairs. A remarkably directional force exhibited by angled taper nanohair arrays was showing here with strong shear attachment (~8 N/cm^2) in the gripping

direction and easy releasing(~1.4 N/cm^2) in the reverse direction (pulled against the angled direction of hairs). The smart adhesive presented here would enable the climbing robots, cleaning transport system such as LCD factory and non-residue sticker for future generation. We believe such a novel structure which is a low-cost, brilliant adhesion; highly stable and even self-cleaning is integral and promising for the future using.
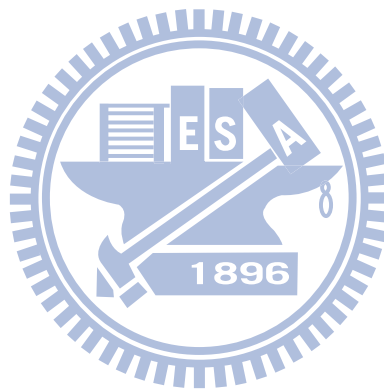
Contents

List of Figures

Schematic mechanism of high CA. (a) High contact angle is induced by nanostructure and low sliding angle caused by nano- and microstructures. (b,c) Illustration of the self-cleaning properties from gecko to taper shape and pillar shape adhesives. It is clearly displaying the air flowing direction which we concerned as the main reason to bring about hydrophobicity.

Phtograph of (a) tape of PUA after replicating and the mold. (b) counter weitht measured system. (c) the high CA of tape after detaching from the glass.

List of Tables

Chapter 1: Introduction

1.1 General Introduction

"There's plenty of room at the bottom" is the title of a classic talk given on December 29, 1959, in which the great physicist Richard Feynman introduced a new field of physics to the annual meeting of the American Physical Society at the California Institute of Technology. Over 40 years ago, Feynman imagined a new physical world of ultra-small volumes and highlighted some difficulties that researchers might encounter when visiting it. His talk provided a vision for engineers and scientists to establish a new field, which—with subsequent developments in novel equipment and manufacturing skills—is now known as "nanotechnology."

In recent years nanotechnology has become one of the most important and exciting forefront field in physics, chemistry, engineering and biology which the characteristic dimensions are below ca. 1000 nm. It shows great promise for providing us in the near future with many breakthroughs that will change the direction of technological advances in a wide range of applications. This kind of work is often called nanotechnology. Sub-micron lithography is clearly very profitable—ask anyone who uses a computer—but it is equally clear that conventional lithographic techniques will not let us prepare semiconductor devices in which individual dopant atoms are located at specific lattice sites. Although computer hardware capability has exhibited steady exponential growth for the last 50 years—and there is a fairly widespread belief that these trends are likely to continue for at least several more years—conventional lithographic techniques are beginning to reach their limits.

As semiconductor devices become scaled down to ever-smaller sizes within the nano-regime, a variety of technological and economic problems arise, the rules of

classical physics give way to quantum mechanics, and the term "molecular-scale" becomes more accurate than "nanoscale." At this point, the scaling of sizes that has successfully reduced device features from the microscale to the nanoscale reaches its limits, and, therefore, alternative manufacturing methods, materials, device structures, and architectures are required.

1.2 Biomimetics

Nature has gone through evolution over the 3.8 G year since life is estimated to have appeared on the Earth [1]. Nature has evolved objects with high performance using commonly found materials. These function on the macroscale to the nanoscale. The understanding of the functions provided by objects and processes found in nature can guide us to imitate and produce nanomaterials, nanodevices and processes. On nanoscale, many of the atoms are still located on the surface, or one layer removed from the surface, as opposed to the interior. Thus, different properties are observed on this scale due to the interface that is not observed in the bulk or individual atoms. Since the properties depend on the size of the structure, instead of the nature of the material, reliable and continual change can be achieved using a single material [2]. As to nanoscale structure, nature is the best teacher giving from God. Biologically inspired design or adaptation or derivation from nature is referred to as 'biomimetics'. It means mimicking biology or nature and is defined as 'the study of the formation, structure or function of biologically produced substances and materials and biological mechanisms and processes especially for the purpose of synthesizing similar products by artificial mechanisms which mimic natural ones'. Nature uses commonly found materials, and properties of the materials and surfaces result from a complex interplay between the surface structure and the morphology and physical and chemical properties. Many materials, surfaces and devices provide multifunctionality.

Molecular-scale devices, superhydrophobicity, self-cleaning, drag reduction in fluid flow, energy conversion and conservation, high adhesion, reversible adhesion, aerodynamic lift, materials and fibers with high mechanical strength, biological self-assembly, antireflection, structural coloration, thermal insulation, self-healing and sensoryaid mechanisms are some of the examples found in nature that are of commercial interest.

There are three areas had grab the eyes from academic and commercial field include cleaning surface, optics and adhesion. The most familiar object within the surface cleaning area for us is Lotus absolutely. The surface of lotus leaves has two levels of microscopic roughness (Fig. 1.1). This hierarchical roughness along with a hydrophobic wax coating makes the lotus leaves superhydrophobic [3-4]. A water droplet forms a large contact angle with low contact angle hysteresis. This results in the water droplets rolling off the surface, leaving the surface clean.
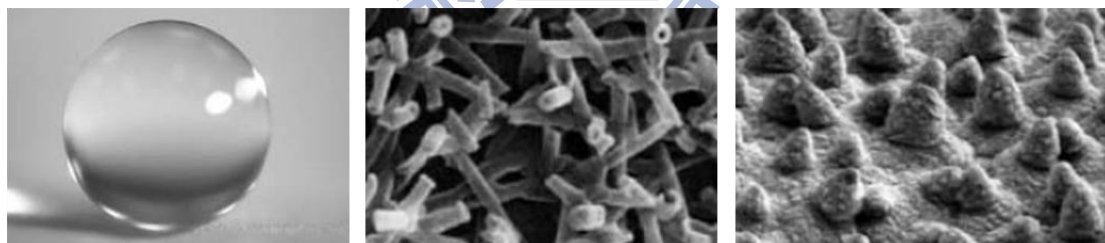
Figure 1.1 Water on the surface of a lotus leaf and the microscopic image of the surface of a lotus leaf.

Moth eyes are the elite in optics area. Bernhard & Miller discovered that the outer surface of the facet lenses in moth-eyes consists of an array of cuticular protuberances termed corneal nipples. Moths use hexagonal arrays of nonclose-packed (NCP) nipples as antireflection coatings (ARCs) to reduce reflectivity from their compound eyes [5-6, 8] (Fig. 1.2). The outer surface of the corneal lenses of moths consists of

NCP arrays of conical protuberances, termed corneal nipples, typically of sub-300nm height and spacing. These arrays of subwavelength nipples generate a graded transition of refractive index, leading to minimized reflection over a broad range of wavelengths and angles of incidence [7]. Accordingly, it increases the transmittance, and therefore the initial interpretation of the nipple array was that it helps to enhance the light sensitivity of the light-craving moths.
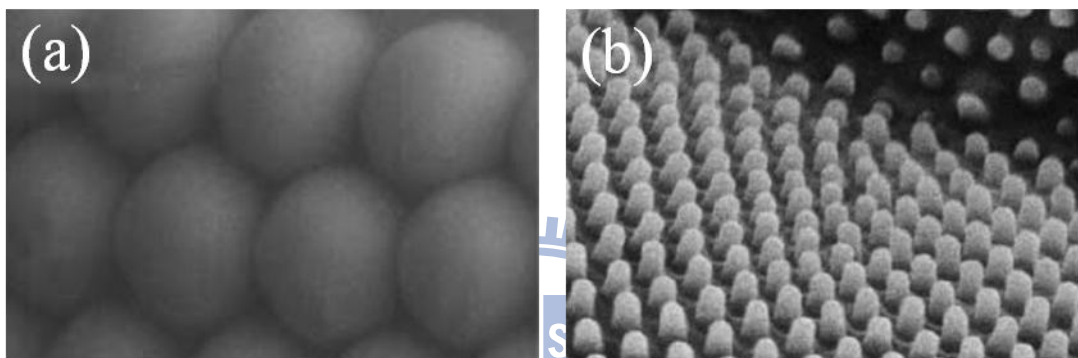
Figure 1.2 SEM images of (a) HCP micro hemispheres and (b), hexagonally NCP nanonipples covering an ommatidial surface.

A gecko is the largest animal that can produce high (dry) adhesion to support its weight with a high factor of safety. The secret of the gecko's adhesive properties lies in the microstructure and nanostructure of gecko feet [9-10]. Microscopy shows that gecko feet are covered with millions of small hairs called setae, which further divide into hundreds of smaller spatulas (Fig. 1.3) [11]. When such a structure is placed against any surface, hairs adapt and allow a very large area of contact with the surface. The van der Waals interaction between approximately millions setae and the substrate after contact is sufficient for the gecko to adhere and allow them to climb vertical surfaces at speeds of over 1 m, with the capability to attach or detach their toes in milliseconds. It has been suggested that this same hairy carpet on the gecko feet also

plays an important role in self-cleaning [12].
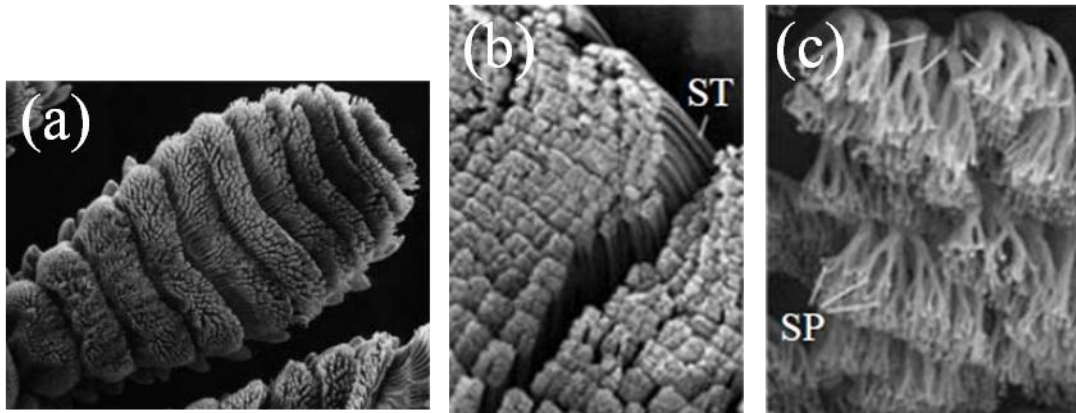
Figure 1.3 (a) a gecko toe. Each toe contains hundreds of thousands of setae and each seta contains hundreds of spatula. SEM micrographs (at different magnifications) of (b) the setae (ST) and (c) the spatula (SP).

Gecko foot-hair, moth eyes and lotus surface mimicking structure were reported in "Nature" and "Science" in the past several times which we will have review next chapter. that shows a way to manufacture a prototype such as gecko-tape made by microfabrication of dense arrays of flexible plastic pillars with self-cleaning, re-attachable, the geometry of which is optimized to ensure their collective adhesion as shown in Fig. 1.3 which proves that the re-attachable dry adhesives based on the gecko principle can find a variety of applications.

The emerging field of biomimetics is already gaining a foothold in the scientific and technical arena. It is clear that nature has evolved and optimized a large number of materials and structured surfaces with rather unique characteristics. As we understand the underlying mechanisms, we can begin to exploit them for commercial applications.

1.3 Hybrid characteristics tape

Over the past few years, adhesive tapes had developed well but not enough to satisfy all. The traditional tapes are allegedly invented by the Germy Beiersdorf from a kind of polymer for hospital using in 1882. Well over decades ago, the year of 1930 can be regard as the milestone of the plastic tape, a staff from 3M named Richard Joe had invented a brand new Scotch adhesive tape bring a great reputation and establish foundation in their business field firmly. Scotch adhesive tape featured in its thin, transparent and good elastic property, becoming the sparkling star beyond their imagine without any doubt, says an exuberant manager from 3M after they became the ludicrous company. Lately, benefited from academic and industrial perennial research, a variety of functional tapes became available, such as the pressure sensitive, water activated, heat activated and drywall tape. However, people are still seeking a hybrid product can be reusable, easy-cleaning and sticky also. Instead of traditional coating on the tape, a resounding inspiration from gecko has revealed a new way to approach modern adhesives which contain both sticky and cleanable property. Microscopy makes gecko's foot isn't as enigmatic as we thought anymore, showing that gecko feet are covered with millions of small hairs called setae, which can induce giant adhesion by van der Waals interaction. Reusable property and high adhesion are the two biggest advantages; even self-cleaning effect as a hybrid function. Gecko's unique features remind human that the ingenious design from   creatures is worthy to research and emulate. The hybrid products with gecko mimicking structure will be avant-garde in next decade.

Chapter 2: Literatures Review

2.1 Fabricated anodic alumina porous

Nanoporous anodic aluminum oxide (AAO) formed by anodization has been widely studied in more than 100 years [1-7]. Porous alumina membranes are used for the fabrication of composites in nanometer scale because of their relatively regular structure with narrow size distribution of pore diameters and interpore spacings [1]. The pore structure is a self-ordered hexagonal array of cells with cylindrical pores of variable sizes with diameter of 25 nm to 420 nm [8] with depths exceeding 100 mm depending on the anodizing conditions used. Essentially, the structure is a result of several coupled phenomena. One mechanism is a nonuniform electric field and, hence, current that arises in the porous aluminum structure as a result of topological variations. The second mechanism is either field-enhanced dissolution or increased local temperature that enhances dissolution of the bottom oxide barrier layer [1]. These coupled phenomena preferentially remove the oxide at the bottom of the pores while leaving the pore walls intact. In another hand, "Nature" describes a model of AAO growth based on simple concepts of volume and charge conservation, coupled with experimentally validated descriptions of interfacial reactions and transport processes recently [9]. The resulting structure is an ordered hexagonal array of cells with cylindrical pores with cell walls composed of alumina. Nanoporous anodic aluminium oxide with self-organized hexagonal arrays of uniform parallel nanopores has been used for various applications in the fields of sensing, storage, separation, and the synthesis of one-dimensional nanostructures [10-12]. Self-ordered AAOs have been obtained by mild anodization (MA) and hard anodization (HA). Both of their advantages are utilized in our experiments.

2.1.1 Mild anodization

In ordinary two-step mild anodization (MA) process, the self-ordered columns of alumina nanopores can be obtained within three well-known growth regimes:

(1) Sulphuric acid (H_2SO_4) at 25 V for D_{int} (interpore distance) = 63 nm [13, 8]

(2) Oxalic acid ($H_2C_2O_4$) at 40 V for D_{int} = 100 nm [14-16]

(3) Phosphoric acid (H_3PO_4) at 195 V for D_{int} = 500 nm [16-17]

Applied voltages higher than the optimum value required to maintain stable anodization in a given electrolyte always result in 'breakdown' or 'burning' of the oxide film caused by catastrophic flow of electric current [18]. Therefore, a long anodizing time (16 h) was required to obtain highly ordered AAO films, as shown in Fig. 2.1 [13]. Masuda et al. [14] reported self-organized pore growth, leading to a densely packed hexagonal pore structure for certain sets of parameters. The self-organized arrangement of neighboring pores in hexagonal arrays can be explained by any repulsive interaction between the pores.
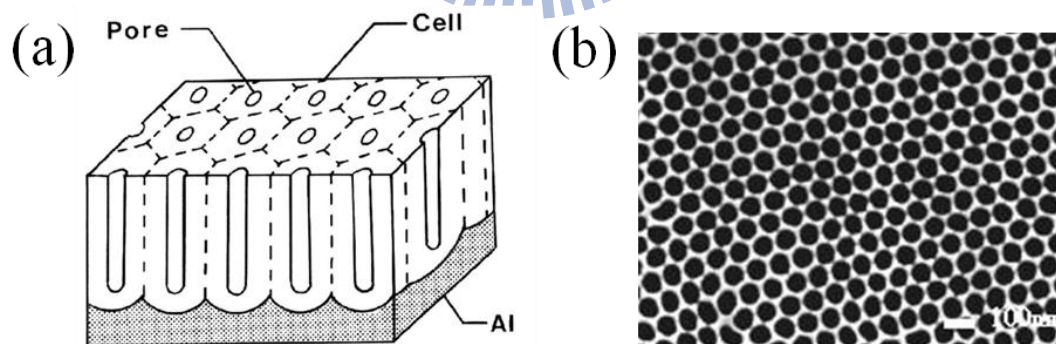
Figure 2.1 (a) Schematic drawing of the idealized structure of anodic porous alumina. (b) SEM micrographs of the bottom view of anodic alumina layers. Anodization was conducted in 0.3 M oxalic acid at 1 °C at 40 V.
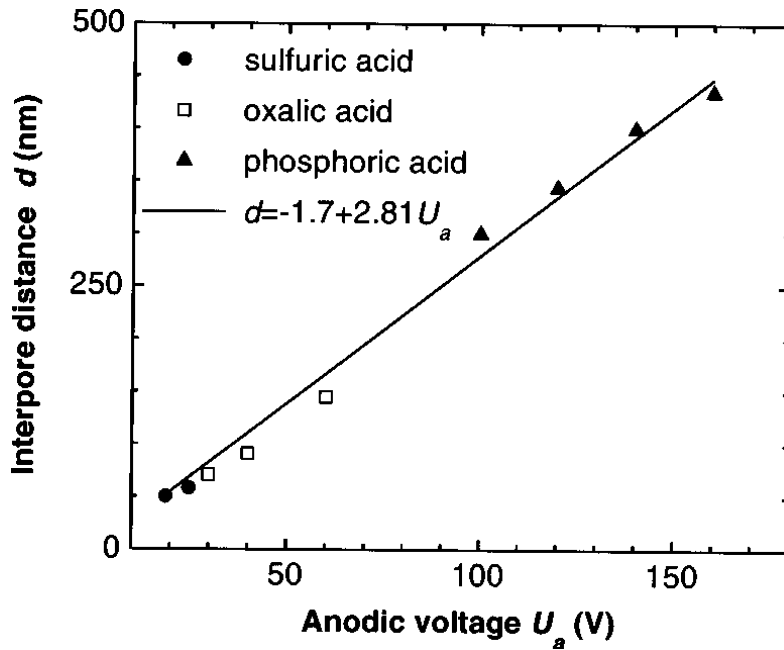
Figure 2.2 Relation between self-ordering voltages and corresponding interpore distance (*d*) in sulphuric (filled black circle), oxalic (squares) and phosphoric acid (filled black triangle).

Fig. 2.2 shows the relationship between interpore distance and the anodic voltage [19]. When the anodization process is outside the self-ordering regimes, the degree of spatial order decreases drastically. Both the barrier-type and pore-type AAO usually start from fairly smooth aluminum surface, but with pits formed at lattice imperfections or by electropolishing [15].

2.1.2 Hard anodization

In general, the fabrication of self-ordered Al_2O_3 pore arrays, under conventional so-called 'mild anodization' (MA) conditions, requires several days of processing time and the self-ordering phenomenon occurs only in narrow process windows, known as 'self-ordering regimes' [8, 13-17]. Owing to the slow oxide growth rates (for example: 2–6 μm h^{-1}), MA processes based on Masuda's approach have not been

used in industrial processes so far. Hence hard anodization (HA) of aluminum, a faster process that was invented in the early 1960s [20-21] is an attractive alternative. HA is carried out at relatively low temperatures and high current densities, and has routinely been used in the aluminum industry to produce anodic films of high technical quality at an efficient rate of production (typically 50–100 μm$\cdot$h^{-1}).

Above all, from a practical point of view, the HA process has many advantages over conventional MA. The major findings on the HA process are as follows. (1) The current density (that is, the electric field strength E at the pore bottom) is an important parameter governing the self-organization of oxide nanopores in a given anodization potential as shown in Fig. 2.3. (2) A new self-ordering regime is established over a broad range of D_{int} = 200–300 nm in $C_2H_2O_4$ and D_{int} = 320 nm in H_3PO_4-H_2O-C_2H_5OH as shown in Fig. 2.4 [22]. (3) The ratio ζ of the D_{int} to the anodization potential is lower (ζHA = 2.0 nm V^{-1} for HA, and ζMA = 2.5 nm V^{-1} for MA) as shown in Fig. 2.5. (4) The porosity P is lower (PHA ~3%, PMA ~10%). (5) The growth rate of the porous oxide film is 25–35 times larger (>50 μm h^{-1}) than for MA as shown in Fig. 2.6. (6) .Ideally ordered alumina membranes with a high aspect ratio (>1,000) of uniform nanopores can be fabricated by HA of pre-patterned aluminum. (7) Pulse anodizations of aluminum were conducted under potentiostatic conditions by using sulfuric acid or oxalic acid. Pulses consisting of a low-potential pulse followed by a high-potential pulse were applied to achieve alternating MA and HA conditions. A combination of HA and MA allows modulation of the pore diameter over extremely high aspect ratios in Fig. 2.7 [18,23].
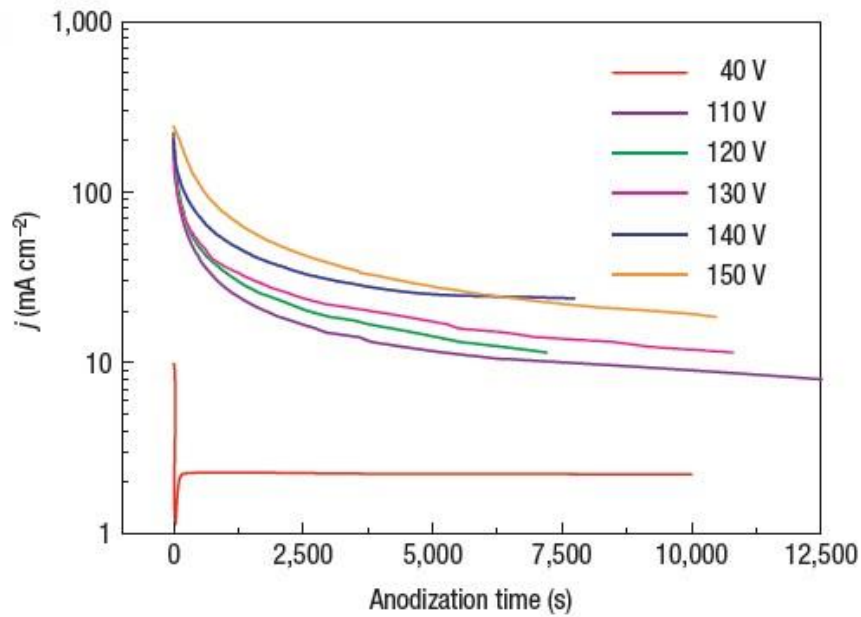
Figure 2.3 Current–time transients during HA of electropolished aluminium substrates in 0.3M $H_2C_2O_4$ (1°C). The current–time transient of a conventional MA (0.3M $H_2C_2O_4$, 1°C, 40 V) is also plotted (red line) for comparison.
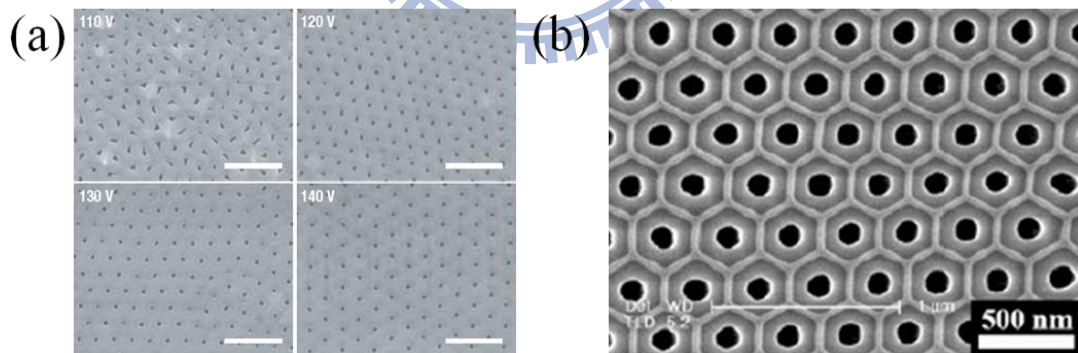
Figure 2.4 SEM micrographs of self-ordered AAOs formed in HA. (a) HA of a mirror-finished aluminium substrate carried out using 0.3M $H_2C_2O_4$ (1°C) for 160 min. (scale bars = 800 nm) (b) HA of a mirror-finished aluminium substrate carried out using 0.4M H_3PO_4 (-10°C, 4000 A m^{-2}).
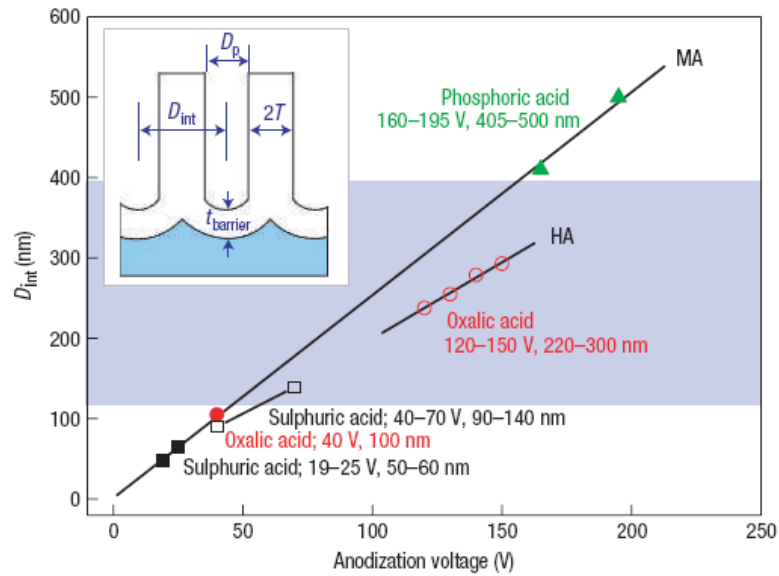
Figure 2.5 Self-ordering voltages and corresponding interpore distance (D_{int}) in conventional MA. The interpore distance (D_{int}) versus anodization voltage observed in oxalic HA is plotted (red open circles) with the corresponding regression line (black solid line). The inset shows the schematic cross-section of the porous alumina structure with the barrier layer; D_p = pore diameter, T = thickness of the pore wall, $t_{barrier}$ = thickness of the barrier layer.
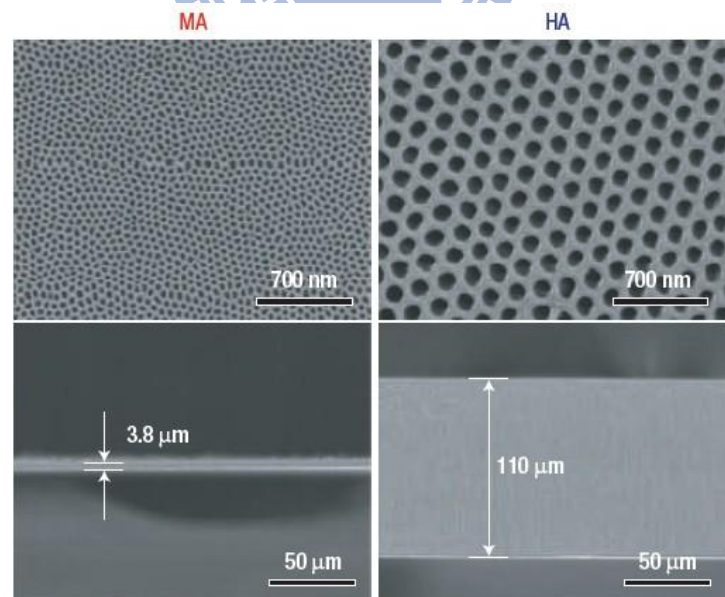
Figure 2.6 SEM micrographs of the corresponding AAO specimens formed by MA for 2 h (left column) and HA for 2 h (right column).
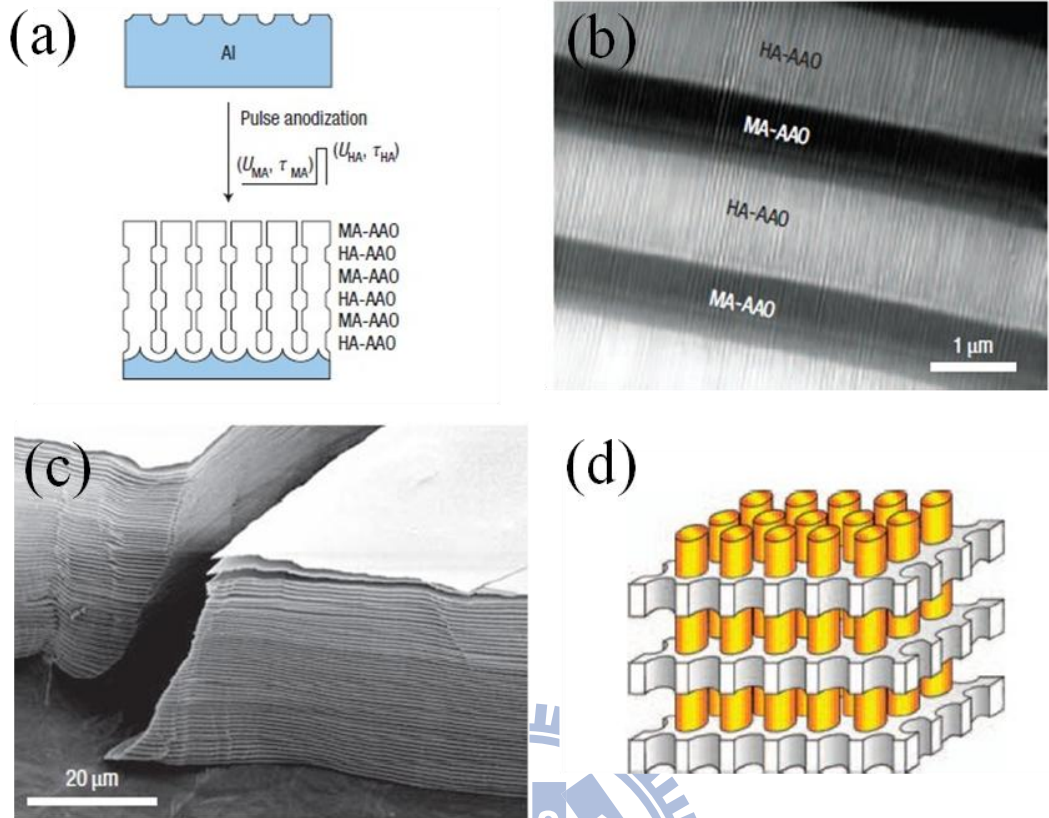
Figure 2.7 (a) Scheme for the fabrication of AAO with modulated pore diameters by pulse anodization. (b) Cross-sectional TEM images of AAO formed by pulse anodization using 0.3 M H_2SO_4 (U_{MA} = 25 V, τ_{MA} = 180 s, U_{HA} = 37 V, τ_{HA} = 1 s), showing modulated pore diameter. Dark and bright image contrast areas correspond to MA- and HA-AAO segments, respectively. (c) SEM image of 3D stacks of MA-AAO slabs. The entire MA-AAO segment slabs were delaminated from an as-prepared AAO by selective removal of HA-AAO segments using 5 wt% H_3PO_4 (45℃). (d) Idealized structure of the composite microstructure.
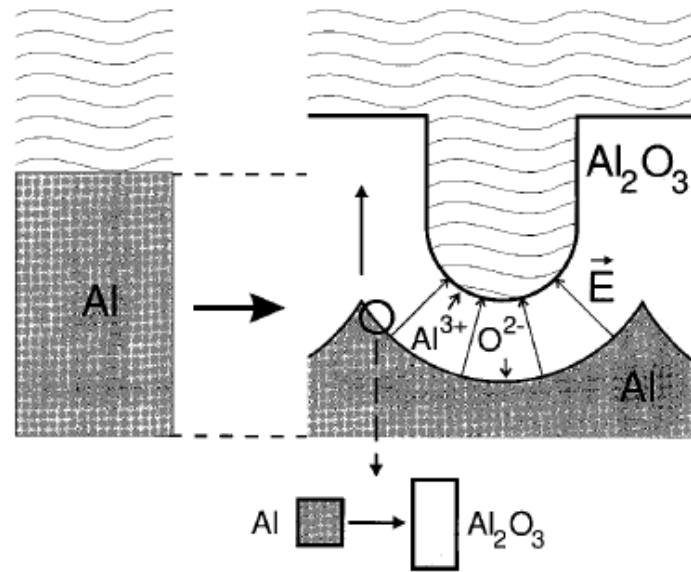
Figure 2.8 Expansion of aluminum during anodic oxidation. On the left the level of the unoxidized metal surface is depicted.

These results imply that pore initiation and the steady growth of alumina cells are strongly influenced by the high current density. In order to explain the mechanism behind pore formation phenomenon of self-organization in HA mechanism, the situation during steady state pore growth has to be considered in Fig. 2.8. Pores grow perpendicular to the surface with the equilibrium of field-enhanced oxide dissolution at the oxide/electrolyte interface and oxide growth at the metal/oxide interface [24]. While the latter is due to the migration of oxygen containing ions (O^{2-}/OH$^-$) from the electrolyte through the oxide layer at the pore bottom, Al^{3+} ions which simultaneously drift through the oxide layer are ejected into the solution at the oxide/electrolyte interface. The fact that Al^{3+} ions are lost to the electrolyte has been shown to be a prerequisite for porous oxide growth, whereas Al^{3+} ions which reach the oxide/electrolyte interface contribute to oxide formation in the case of barrier oxide growth [25]. A possible origin of forces between neighboring pores is therefore the mechanical stress which is associated with the expansion during oxide formation at

14

the metal/oxide interface. During the initial stages of film growth, the penetration paths that develop   (which are the precursors of the regular pores) are more densely distributed due to the high anodizing current densities. Since the oxidation takes place at the entire pore bottom simultaneously, the material can only expand in the vertical direction, so that the existing pore walls are pushed upwards. Thereafter, steady film growth is attained with the development of the major pores and the repulsive interaction between the alumina cells. The repulsive interaction force, which is associated with expansion during film formation at the aluminium/oxide interface [26], increases with electric field. The strong repulsive or expansion force (high field) under high current density limited the transverse growth of alumina cells and forced them to form close-packed hexagonal arrays as shown in Fig. 2.9, thus producing highly ordered AAO films over a large area [27].
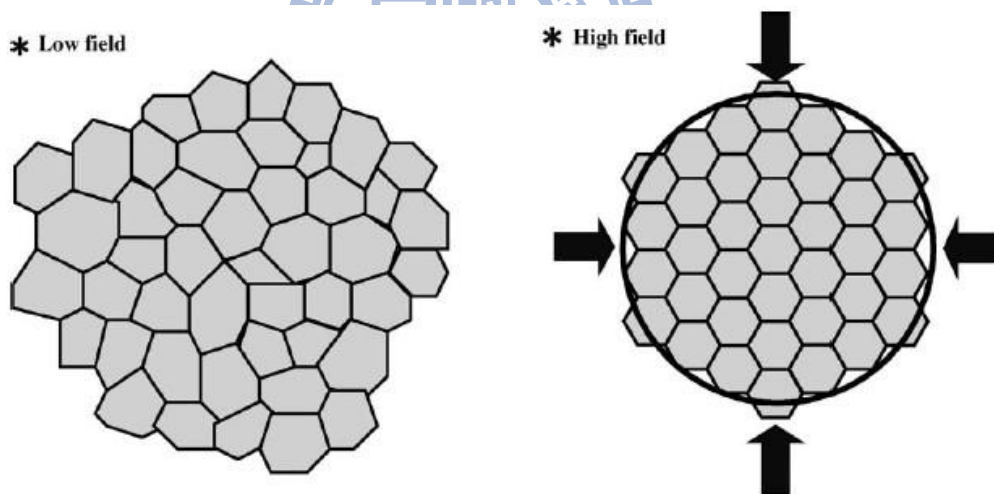
Figure 2.9 Schematic representation of self-organization of cell arrangement at high-current-density and low-current-density.

2.1.3 Taper AAO

The anodic porous alumina, which is formed by Al anodization in acidic solution, is a typical self-ordered material. Under appropriate anodization conditions,

15

long-range-ordered anodic porous alumina with an ideally pore size can be obtained.

The shape of the holes in the anodic porous alumina can be controlled by a process

composed of a series of anodization and subsequent etching treatments (H_3PO_4) as

shown in Fig. 2.10. By using the anodic porous alumina with shape-controlled holes

as a mold for the replication, the preparation of AR structures of polymer could be

achieved [28].
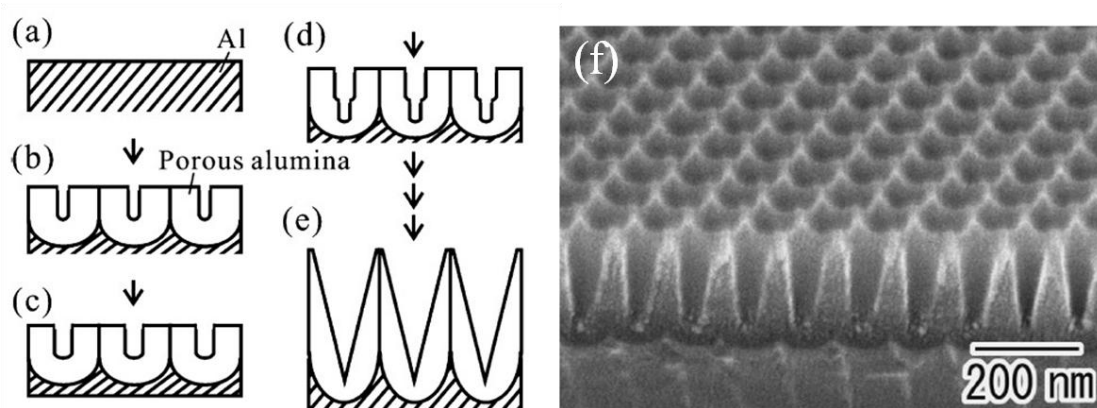
Figure 2.10 Schematic for preparation of anodic porous alumina mold with tapered

holes. Al substrate (a) anodization (b) pore widening (c) second anodization (d) and

porous alumina with tapered holes (e,f) SEM image of anodic porous alumina with

tapered holes using oxalic at 40 V.

2.2 Nondestructive replication of master mold

Nondestructive replication usually contains two methods. One is thermal curable include hot embossing like PMMA which is relatively "hard" and casting like PDMS [29], another one is photo- or UV- curable material like polyacrylate [30] which may contain the photo initiator.

Microcontact printing and molding have several important advantages over other techniques for the transfer of patterns. First, this transfer is not subject to a diffraction limitation, providing access to sub-micrometer features without complicated optical or electron-beam lithography. Second, application of the stamp is direct and simple. Pattern transfer occurs simultaneously over the entire surface of the stamp, allowing a high speed of transfer compared to electron-beam or scanning-probe methods, while having a resolution approaching that of these techniques. Third, the flexibility of elastomers allows their application to non-planar substrates not obviously patternable by other techniques [31].
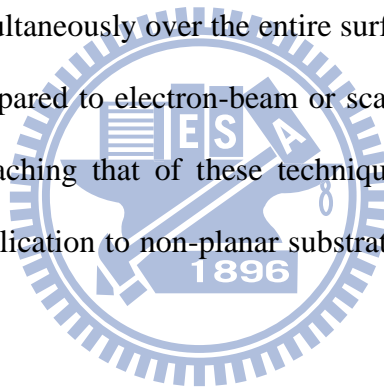
2.2.1 PDMS

Poly(dimethylsiloxanes) have a unique combination of properties resulting from the presence of an inorganic siloxane backbone and organic methyl groups attached to silicon. They have very low glass transition temperatures and hence are fluids at room temperature. These liquid materials can be readily converted into solid elastomers by cross-linking as shown in Fig. 2.11 [32].
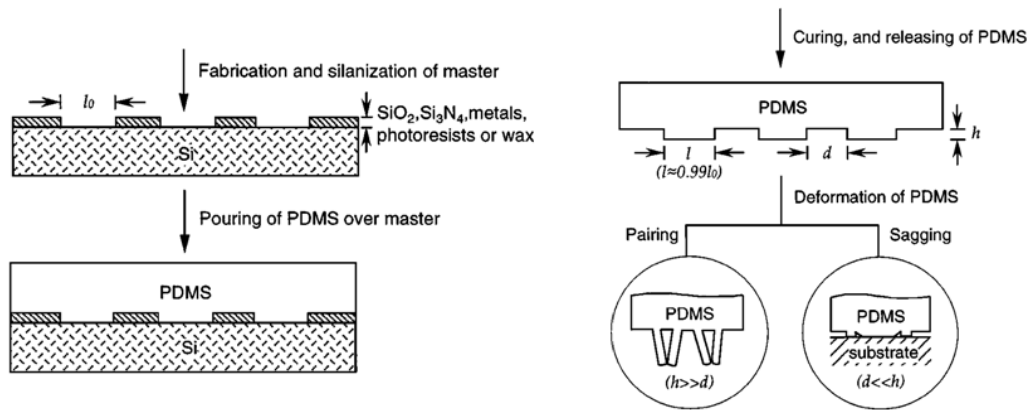
Figure 2.11 Schematic illustration of the procedure for fabricating PDMS stamps from a master having relief structures on its surface.

Soft lithographic techniques with PDMS are currently most useful for patterning features and for fabricating structures on the size scale of 500 nm and larger. The extension of these methods to produce structures in the sub-100-nm range is limited in part by the low elastic modulus of the form of poly(dimethylsiloxane) most commonly used in fabricating stamps (Sylgard 184 PDMS) [33]. Furthermore, there's a approach called soft-mold-induced self-construction (SMISC), which use both electrostatic forces and surface tension difference, to facilitate the pattern growth by microwave as shown in Fig. 2.12 [34].
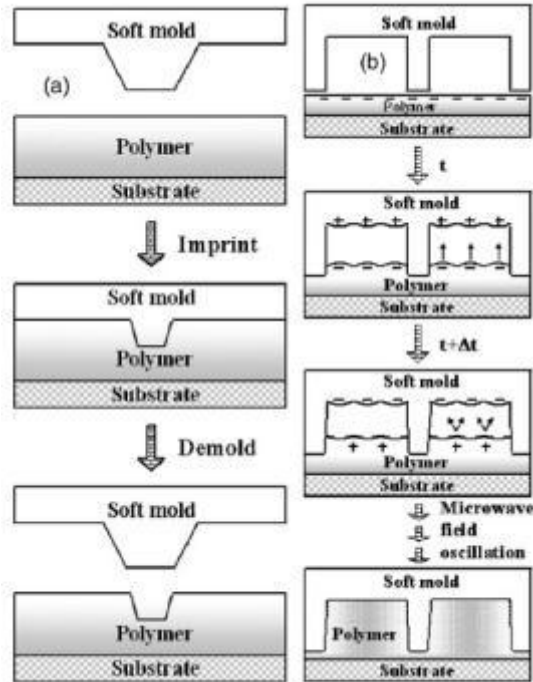
Figure 2.12 Schematic illustration of (a) soft mold imprinting under a force field and (b) SMISC by microwave.

2.2.2 PUA

Polyurethane acrylate (PUA) is a modulus-tunable ultraviolet curable mold that can provide a rigidity high enough for fine and dense features with a high aspect ratio and yet a degree of flexibility for a conformal contact over a non-flat, large area. The mechanical properties of the mold can be tailored by the chain length of an acrylate modulator in the cross-linking reaction. This tunability can be utilized to obtain a proper balance that is needed for a given patterning technique between the rigidity requirement (tensile modulus = 320 MPa) of a mold for patterning a fine structure and the flexibility requirement (tensile modulus = 19.8 MPa) for a conformal contact. The UV-curable mold consists of a functionalized prepolymer with acrylate group, a photoinitiator, and a radiation-curable releasing agent for the surface activity. Fig. 2.14 [35] gives the chemical formulas of the species involved and the reaction route to preparing the mold material. The excellent characteristic properties of the mold

suggested in this study are a result of the fact that the prepolymer contains both cycloaliphatic and linear long chains. The former provides the rigidity while the latter does the flexibility.
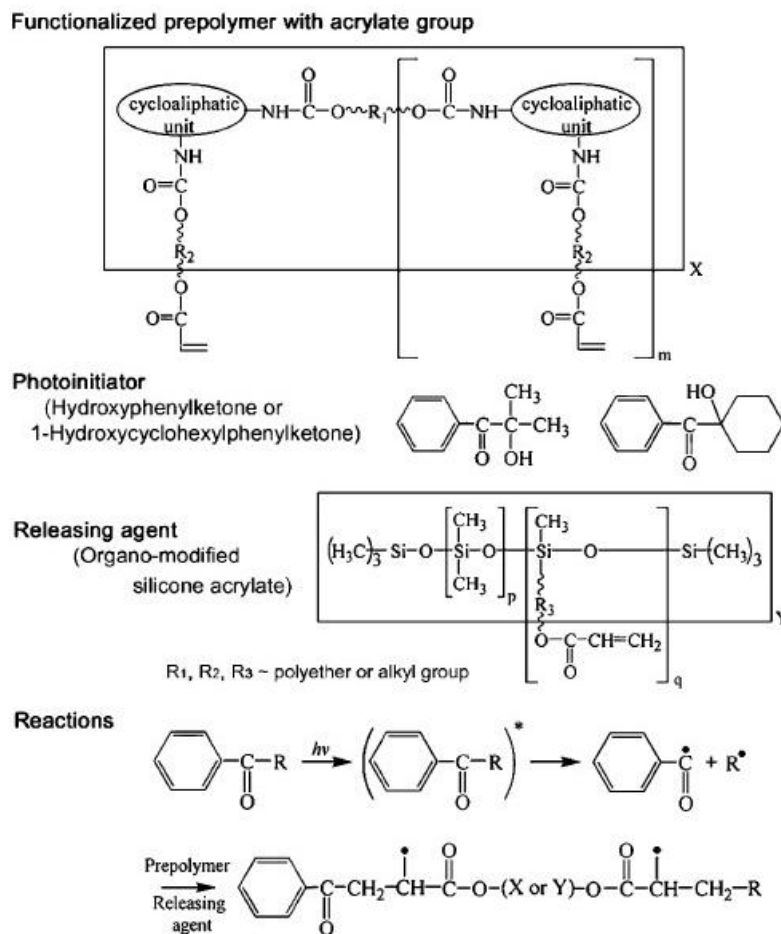
Figure 2.14 Preparation of a UV-curable mold and reaction route.

Most polymer materials are brittle materials, which fail at small values of strain, which means the polymer will break instantly once the ratio of stress to strain across over the tensile modulus(Young's Modulus). The mechanical properties of the two types of PUA molds, hard and soft, were determined by universal testing machine (UTM, LR10K, Lloyd Instruments, England) with the molds prepared in the form of

nonpatterned sheets for the tensile modulus and elongation at break. As shown in the Table 2.1 and Fig. 2.15 [30], the usual PDMS of Sylgard 184 has a good elongation property that allows excellent processing characteristics such as spontaneous wetting. On the other hand, the modulus is too low to support the mold structure in sub-micrometer range, typically for dense or high-aspect-ratio patterns.
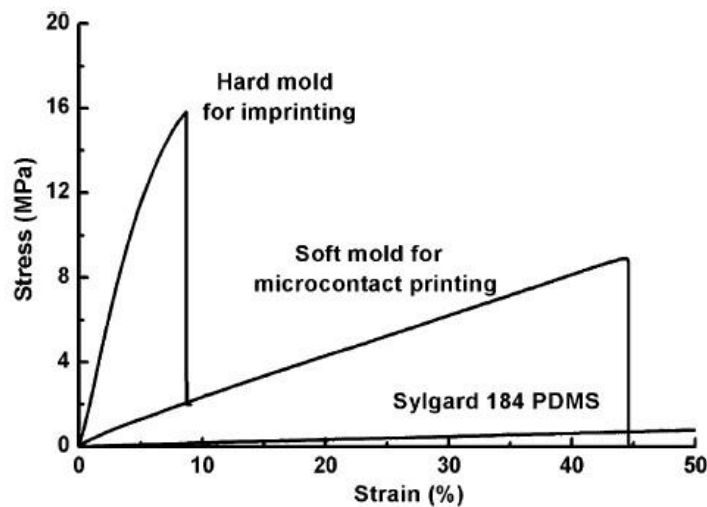
Figure 2.15 Tensile stress-strain relationships of three materials from the UTM analysis.

material	tensile modulus (MPa)	elongation at break (%)
hard PUA mold for imprinting	320	9
soft PUA mold for contact printing	19.8	45
Sylgard 184 PDMS	1.6	146

Table 2.1 Comparison of tensile modulus and elongation at break for three materials.

To enhance the mechanical integrity and thereby extend the patterning capability to smaller feature sizes, a modified hard PDMS (tensile modulus = 8.2 MPa, elongation at break = 7%) [36-37] has been introduced. Nevertheless, comparison of

the mechanical properties of the soft PUA mold in Table 2.1 and those of the hard PDMS mold suggests that the conformal contact should be better because the soft PUA is much more flexible, despite its higher tensile modulus, due to its higher elongational property than that of hard PDMS. On the other hand, the high modulus of the hard PUA mold in Table 2.1 implies that the mold could withstand the pressure applied for imprinting as shown in Fig. 2.16. Therefore, the material is adequately hard yet flexible enough for molding. In our approach, we utilize the soft PUA as its mechanical property is proper than others.
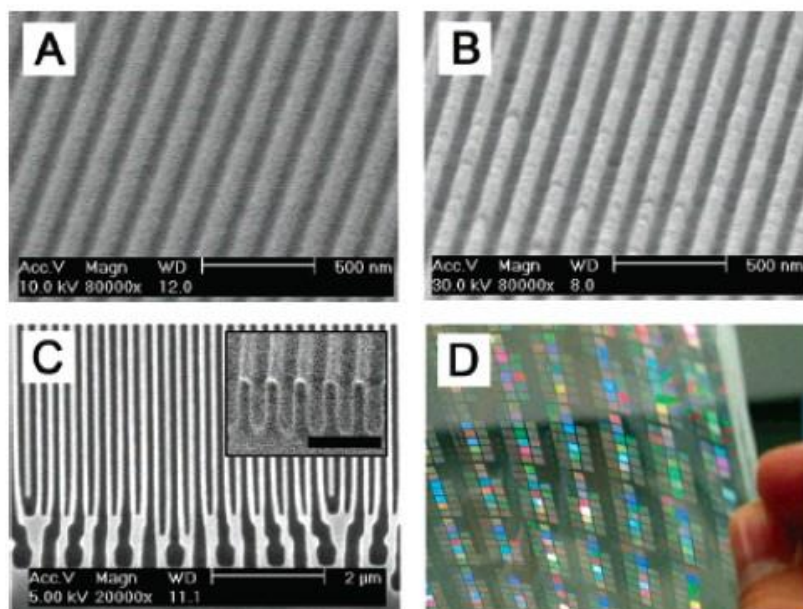
Figure 2.16 SEM and optical mocroscopic images of replication results. (a) Master pattern of 75-nm line/space polarizer, (b) Replicated pattern of (a). (c) Replicated pattern of a 100-nm line/space circuit pattern. Inset is the cross-sectional SEM image. Bar scale in the inset is 500 nm, and (d) Example of large area replication of hologram gratings.

2.3 Gecko-inspired artificial structure mimicking

Van der Waals forces are unspecific and therefore omnipresent between practically any solid surfaces; the reason why we do not experience them in everyday life is their extremely short range: the surfaces have to be in intimate contact over large areas to exert strong forces. Nature utilizes these forces in animal locomotion. The prime example, which has aroused scientific interest especially over the last decade, is the adhesion and friction of the gecko pad for example during running, climbing, and traversing ceilings. It is now known that the gecko owes its extreme reversible adherence to a fine structure of hierarchically arranged fibrils, which enable it to exploit van der Waals and capillary forces with great efficiency as shown in Fig.2.17 [38-41].
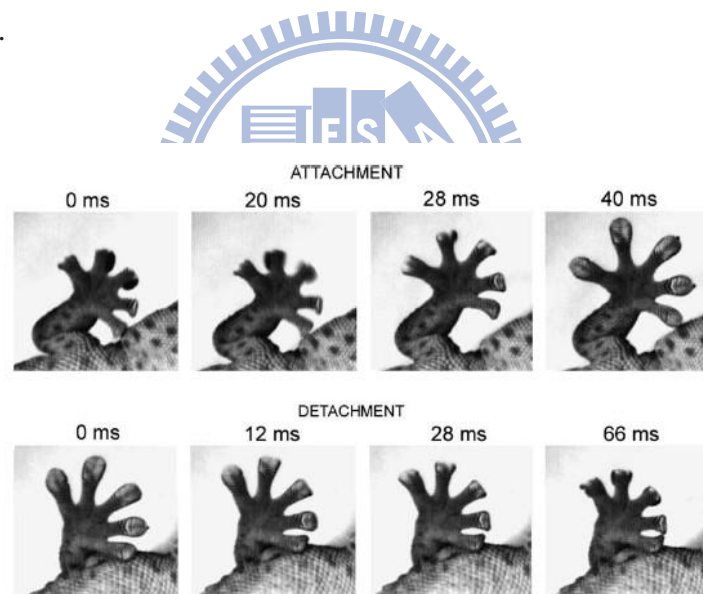
Figure 2.17 Snapshots of gecko attachment and detachment from a glass ceiling. Peeling is used to achieve detachment via special muscles and joint design allowing so-called digital hyperextension.

2.3.1 Dry adhesion

Dry adhesion mechanism in gecko lizards has attracted much attention since it provides strong, yet reversible attachment against surfaces of varying roughness and

orientation. Such unusual adhesion capability is attributed to arrays of millions of fine microscopic foot hairs (setae), splitting into hundreds of smaller, nanoscale ends (spatulae), which form intimate contact to various surfaces by van der Waals forces with strong adhesion (10 N/cm^2) as shown in Fig. 2.18 [38, 40]. Recent advances of nanofabrication via top-down and bottom-up approaches have made it possible to develop synthetic, high-performance dry adhesives based on a range of different materials. Of these, polymeric nanohairs and carbon nanotubes (CNTs) have been largely used as attachment tip materials, since they allow for robust, high aspect ratio (AR) structures in a simple and reproducible manner [44-47, 48-49]. In fact, researchers have already demonstrated that artificial dry adhesives can be applied to climbing robot [50] and biomedical patch [51], as illustrated in Fig. 2.19.
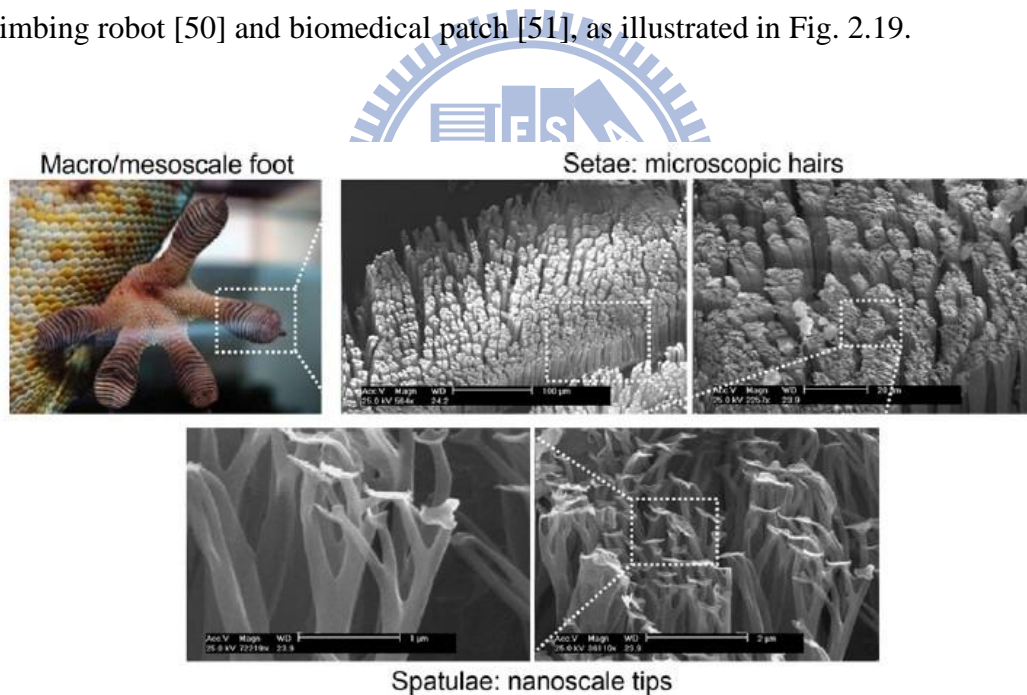
Figure 2.18 Multi-scale combined hierarchical gecko foot hairs. As shown, millions of fine microscopic foot hairs (setae) on the attachment pads split into hundreds of nanoscale ends (spatulae).
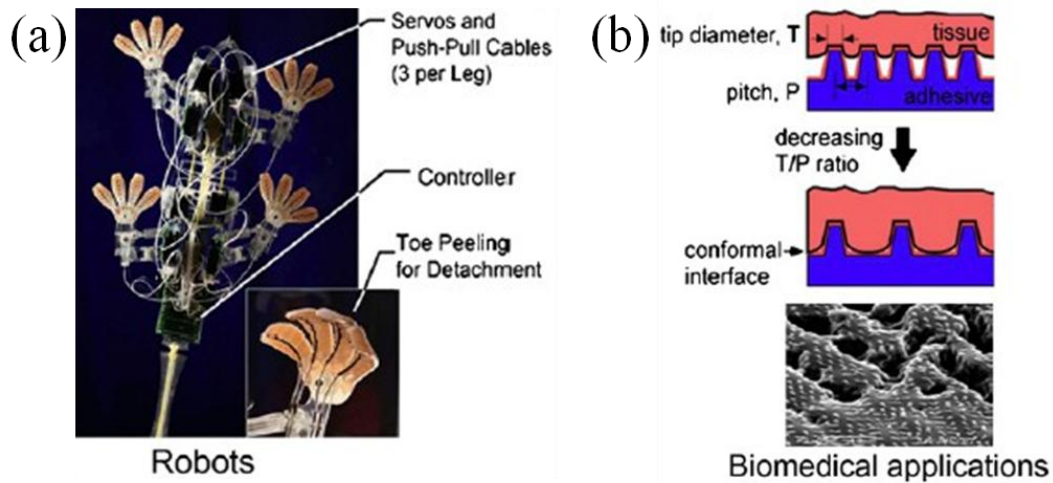
Figure 2.19 Examples of applications of gecko-inspired dry adhesives: (a) a climbing robot and (b) a biomedical patch.

In this section, we aim to provide an overview of recent advances in artificial dry adhesives with nanoscale (submicron) structured materials, with emphasis on polymeric nanohairs and CNTs. A variety of synthetic dry adhesives that are based on the above two materials are outlined with their structural characteristics as well as adhesion properties.

Fabrication methods

For fabricating gecko-inspired artificial dry adhesives, a number of methods have been proposed, which can be classified into two main streams: polymer-based dry adhesives and carbon nanotube (CNT)-based dry adhesives. These two kinds of adhesives have been developed independently by utilizing different fabrication principles (Fig. 2.20). In general, the polymer-based adhesives have been fabricated by a top-down approach. For example, conventional topdown nanofabrication techniques such as electron-beam lithography, photolithography and etching techniques were utilized for fabricating nanohairs directly from a substrate [44]. In

parallel, polymer molding techniques were adopted by using a master with straight

nanoholes [42, 45, 47, 52]. As to CNT-based dry adhesives, a bottom-up approach in

which the CNT arrays were grown from the catalyst layer deposited on a substrate by

chemical vapor deposition (Fig. 2.20) [18-19, 55-56]. Due to different process

characteristics and materials properties used in the fabrication, the polymer-based and

the CNT-based dry adhesives demonstrate different adhesion capability and

parameters, which are summarized in Table 2.2.
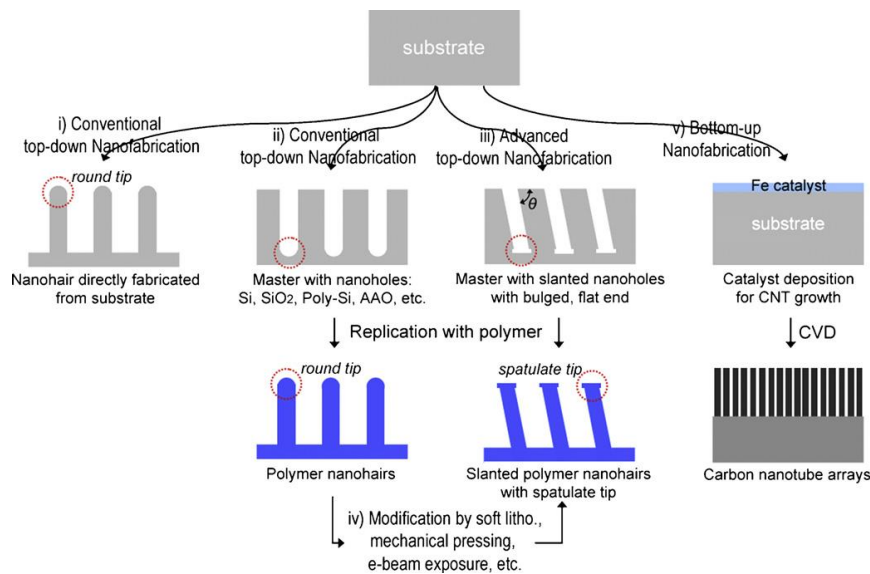
Figure 2.20 A schematic illustration of the classification of five major fabrication

approaches for artificial dry adhesives.

	Polymer-based dry adhesives	CNT-based dry adhesives
Fabrication	• Top-down approach	• Bottom-up approach
Advantages	• Simple and cheap process • Large area fabrication • Scalability • Geometry-controllability • Tunable material properties • Low preload	• High mechanical modulus ($\sim$1000 GPa) • High resolution (diameter: $\sim$10 nm) • High AR ($>10^4$) • Superior adhesion strength
Disadvantages	• Limited mechanical strength ($\sim$1 GPa) • Limited resolution (diameter $>$50 nm) • Limited AR (10—20) • Relatively low adhesion force	• Complicated and costly process • Small patterning area • High preload

Table 2.2 Characteristics of polymer-based dry adhesives and CNT-based dry

adhesives.

One of the biggest advantages of the polymer-based methods is that they offer a simple and scalable approach to fabricating gecko-mimicking nanohairs with tailored geometry (angle, radius, height, shape of tip and hierarchy) and tunable material properties (modulus, surface energy, etc.) in a fast and cost-effective manner. Large area fabrication can be also achievable with the polymer-based approaches. The adhesion strength, however, is usually lower than that of the CNT-based adhesives because the resolution and AR of polymer nanostructures are restricted by low mechanical strength of polymer materials. In contrast, the CNT-based dry adhesives usually have high level adhesion strength since the CNTs have superior structural features such as high AR, extremely small radius (10 nm) and high modulus (1000 GPa) [48-49]. Despite these advantages, the CNT-based methods are potentially limited by complicated process for CNT growth and small patterning area (4mm×4mm) [48, 55]. Several exemplary works are in order to demonstrate how nanofabrication methods have been utilized to achieve synthetic dry adhesive with these two materials.
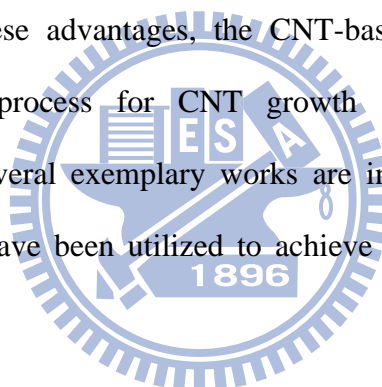
1. Polymer-based dry adhesive:

The gecko's high AR nanohairy structures can maximize the contact area by a large number of pillars at the time of contact and a smaller effective modulus, which in turn increases the adhesion force against various surfaces. To achieve high AR structures, Geim et al. presented a prototype of gecko tape having polyimide nanohairs (as small as 200 nm diameter) fabricated by e-beam lithography [44] (categorized into ''method i'' in Fig. 2.20). By fabricating high AR polyimide hairs (see Fig. 2.21a), relatively high normal adhesion (3 N/cm^2) was obtained. The slow and expensive process of e-beam lithography, however, is a major shortcoming of this approach. In this work, they reported that the flexibility of the substrates was a crucial

factor for obtaining high pull-off force. In these studies, researchers demonstrated that a small thickness of the substrate enhances the actual adhesion significantly as it allows flexibility and equal load sharing and prevents edge stress concentration [57]. After the work by Geim et al., alternative approaches have been developed to overcome the limitations of e-beam lithography. The proposed approaches are mostly based on nanomolding methods, as they allow for a facile process with minimal time and cost. In these methods, various substrates (e.g., Si, SiO_2, poly-Si, AAO, polycarbonate film, etc.) having nanoholes are prepared by e-beam lithography, photolithography, etching or electrochemical reactions. Subsequently, nanohairs are replicated by molding polymers against the substrates, as illustrated in ''method ii'' in Fig. 2.20. As opposed to the ''method i'', the fabricated substrates can be re-used as a template for nanomolding, allowing for significant reduction of time and cost. For example, Majidi et al. reported polypropylene nanohairs (see Fig. 2.21b) [46]. The hairy structures were fabricated by casting polypropylene film into a commercially available polycarbonate filter at an elevated temperature (at 200℃ for 25 min) in a vacuum condition. In spite of high elastic modulus (1GPa) of the polypropylene, the hair arrays exhibited the coefficient of friction greater than 5 N/cm^2 due to the enhanced compliance of the high AR nanostructures. Anodic alumina oxide (AAO) also has been utilized as a mold for generating high AR polymer nanohairs. The AAO template has highly ordered nanoholes whose diameters and depths can be easily controlled by varying the electrochemical parameters without the need of expensive e-beam or photolithography. Cho et al. presented a gecko mimicking adhesives by molding from AAO but with a low adhesion as shown in Fig. 2.21d (0.05 N/cm^2). High AR polymer nanostructures could be easily obtained by simply molding the templates with thermoplastic or UV cured polymers [42, 52]. However, the resulting nanohairs molded from the AAO usually suffer ,from self-matting problem due to wet

chemical etching during template release or too high packing density and AR of the nanostructures, which diminishes the resulting adhesion force significantly [42, 52]. Jeong et al. suggested a nanodrawing method for fabricating high AR polymer nanohairs (80nm diameter, 2 μm height and AR > 20) on a solid substrate by sequential application of molding and drawing of a thin polymer film with 3 N/cm^2 (see Fig. 2.21c) [45].

Hierarchical structures with stacked fibers of different dimensions were recently fabricated by different methods. Well-defined arrays of hierarchical microfibrils were obtained by multistep photolithography using SU-8 [58]. Molding with PDMS via a adequate mold rendered fibrils with AR of 4 (25 μm diameter) on top of fibrils with AR up to 1 (5 μm diameter; Fig. 2.22a) [53, 58]. Two-step molding has also been used to fabricate PU hierarchical structures: the base fibers were formed by softlithography, while the top ones were formed by capillary molding and a second curing step (the first level of fibrils were 5 to 50 mm in diameter and 25 to 100 mm high; the second-level fibers were 350 nm to 3 mm in diameter and 2.8 to 20 mm high; Fig. 2.22b) [59]. Interestingly, these hierarchical hairs maintained their adhesive force even on a rough surface due to an increase in the contact area by the enhanced height of hierarchy, whereas simple nanohairs lost their adhesion strength, demonstrating the usefulness of hierarchical structures against rough surfaces. Nevertheless, most of them reported are without a large enough adhesion and directional force.

Fibrillar surfaces with a slanted angle show smaller effective elastic modulus than planar surfaces. As a result, they deform easily and form contact effectively, especially when adhering to rough substrates. The elastic-strain energy stored in slanted single fibrils during pull-off is dissipated and, as a consequence, the separation work is higher than for a planar contact of similar material [43, 60]. From the point of view of fracture mechanics, fibrillar structures with a slanted angle require frequent

29

re-initiation of the interface crack and the failure of the interface therefore occurs at higher stresses [60]. As shown in Fig. 2.23a, spatular tips at angles between 0 and 90^0 with respect to the substrate were obtained on tilted PU fibers by applying a controlled load to the tilted fibrils during curing, causing bending of the fibrils [54]. This design, containing two independent tilted components (fiber and spatula), represents the most complex structure obtained to date with artificial systems. Slanted fibrillar structures were obtained by double replication of tilted SU-8 fibrillar arrays obtained by photolithography (Fig. 2.23c). This process involved tilted exposure of the resist layer to obtain fibrils forming angles between 0 and 50^0 with the substrate and exhibiting dimensions of 4 to 35 μm in diameter and ARs of up to 10. A mold of silicone rubber containing angled holes is then fabricated by soft-molding against the SU-8 template and subsequently used to obtain PU microfibers from liquid precursors [61]. Alternatively, arrays of PP microfibers were fabricated by first filling PC membranes with PP to obtain vertical fibrils and then tilting them by processing the patterned film through two heated rollers (Fig. 2,23b) [62]. Tilted fibrils with 0.6 mm diameter, 18 to 20 mm length, and a 45° tilting angle were obtained. Coarser structures with 1mm length, 380 μm diameters and a tilt angle of 20° with a top face inclined at 45^0 with respect to the vertical were obtained by casting a PU precursor onto a mold fabricated by micromachining. Tilted structures were also prepared by a post-molding electron-beam irradiation step. The irradiated fibril surfaces shrink more than the opposite surface, resulting in bending of soft-molded fibrils [47]. With this method, PUA nanopillars (100 nm in diameter and with an AR of 10) were fabricated with tilting angles between 30° and 80° (Fig. 2.23d).
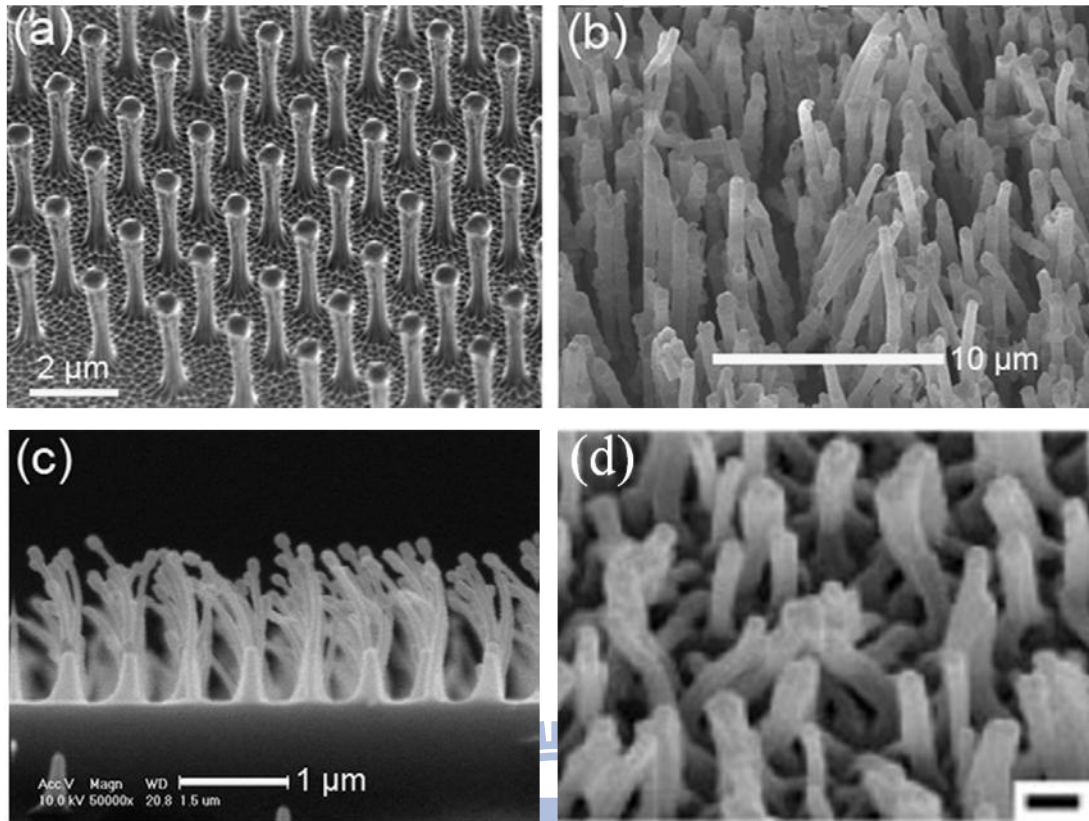
Figure 2.21 SEM images of gecko-inspired high aspect ratio nanostructures by different methods. (a) Polyimide nanohair arrays fabricated by e-beam lithography, (b) Polypropylene nanohairs fabricated by casting polypropylene film into a polycarbonate filter at an elevated temperature, (c) PMMA nanohairs fabricated by sequential application of molding and drawing of a thin polymer film, and (d) h-PDMS nanohairs fabricated by molding from AAO, the scale bar is 500 nm.
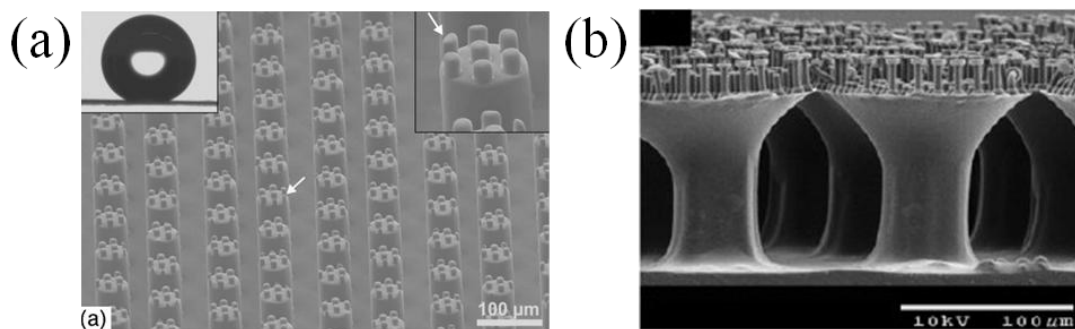
Figure 2.22 (a) An array of hierarchical pillars fabricated by soft molding Sylgard

184 on SU-8 photolithographic templates. The base-pillars have a radius of 25 mm and a height of 200 mm. The top pillars have a radius of 5 mm and an aspect ratio of 1. (b) PU structures with a complex tip geometry prepared by soft-lithography and capillarymolding.
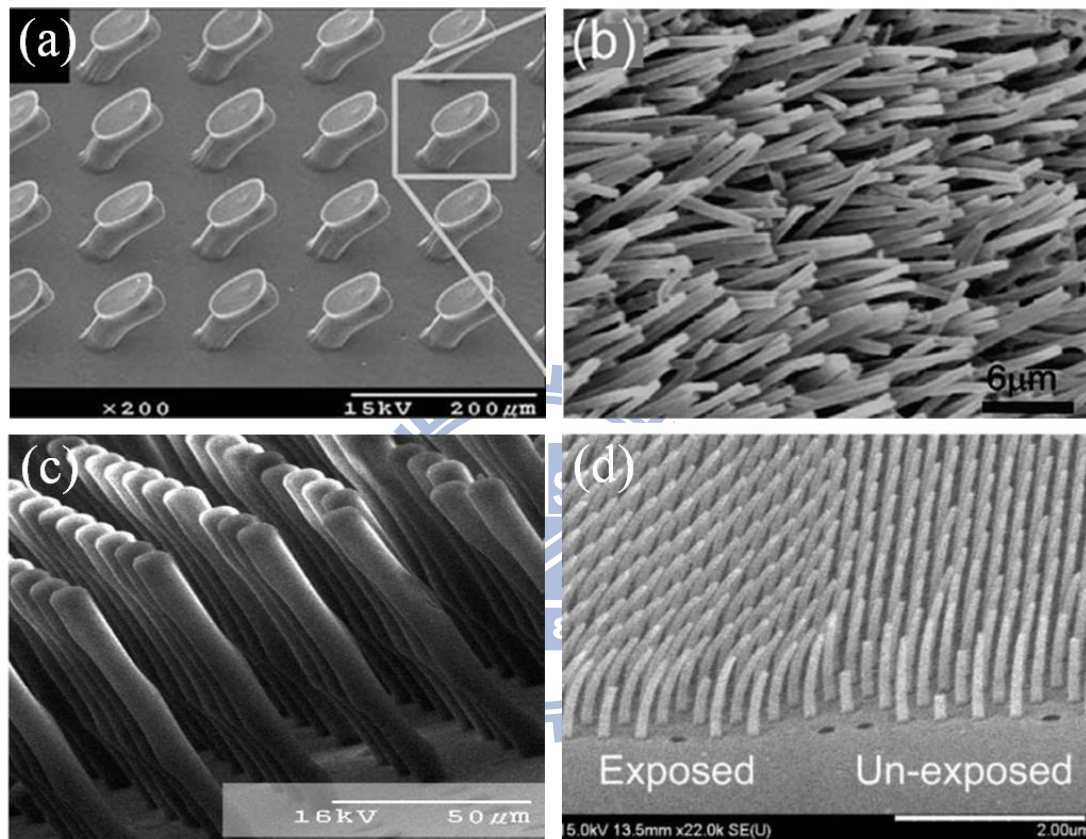
Figure 2.23 Fabrication of tilted fibers and tips: (a) Example of tilted PU microfibers with tilted fiber tips, (b) Angled polypropylene nanohair arrays fabricated by molding and roll pressing, (c) PU fibrils obtained by soft-molding on SU-8 wafers patterned by inclined lithography. The fibrils have a diameter of 8mm, and (d) Tilted PUA nanofibers fabricated by local softening of the polymer using electron-beam irradiation.

2. CNT-based dry adhesives

Ge et al. suggested dry adhesives with micropatterned CNT arrays (Fig. 2.24a

and b) [48]. Interestingly, they reported that micropatterned CNT arrays with optimized geometry have four to seven times higher shear adhesion (~36 N/cm^2) strength than nonpatterned CNT arrays. Moreover, the adhesion strength was maintained over thousands of cycles (Fig. 2.24c). Qu et al. also reported similar adhesion strength (15 N/cm^2 shear adhesion and 30 N/cm^2 normal adhesions) by growing single walled CNTs (SWCNTs) [63]. Following this work, they further enhanced the performance of the dry adhesive using MWCNTs [49]. With use of vertically aligned MWCNT having curly entangled end segment, they could obtain extremely high shear adhesion (~100 N/cm^2), which was ten times higher than gecko's adhesion strength (Fig. 2.24d and e). The strong shear adhesion comes from shear-induced alignment of the nonaligned top layer of the nanotubes enhancing the contact line length (Fig. 2.24e) [49]. As a result, increasing the CNT length greatly enhanced the shear adhesion. In contrast, the normal adhesion force was almost insensitive to the nanotube length as a result of point contact. Interestingly, there have been seemingly opposite reports on repeatability and robustness of CNT-based dry adhesives. Ge et al. and Qu et al. reported that CNT arrays maintained the strength for long attachment/detachment cycles whereas Zhao et al. reported that the adhesion strength was decreased with repeated use due to an interface failure between CNT arrays and the substrate [48-49]. Recently, Wirth et al. investigated the structural changes of vertically aligned CNT arrays (10 nm in diameter and 100 μm in length) after attachment [64]. They observed that the applied force for preloading leads to the collapse of the CNT arrays limiting the repeatable use of the dry adhesives, as shown in Fig. 2.24f. It seems that the interfacial strength between CNTs and the substrate is important for ensuring robustness and repeatability of the CNT-based adhesives. In general, CNT-based dry adhesives have higher adhesion strength than polymer-based adhesives due to outstanding structural properties such as extremely high AR (> 10^4,

diameters around 10nm and heights over 100 μm). With extraordinary high AR, the effective modulus of CNT is reduced below Dahlquist criterion (E ~100 kPa) in spite of its high mechanical modulus (~103 GPa) (see Fig 2.28). However, the patterned area of CNT arrays is usually small (~1.6mm^2) due to the complicated process (photolithography, catalyst deposition and chemical vapor deposition at high temperature, e.g., ~750 °C). It is worthwhile noting in this regard that the adhesion force per area can be enhanced greatly by reducing the contact area [65]. Also, the adhesion force of single nanohair measured by AFM might be misleading as it would not scale linearly into the bulk adhesion strength. In addition to the complicated and expensive process as well as small patterning area, another major concern of the CNT-based adhesives is that it requires a high preload (50~500 N/cm^2) compared to that of polymer-based adhesives (< 0.5 N/cm^2), potentially limiting the widespread use of the CNT-based adhesives.
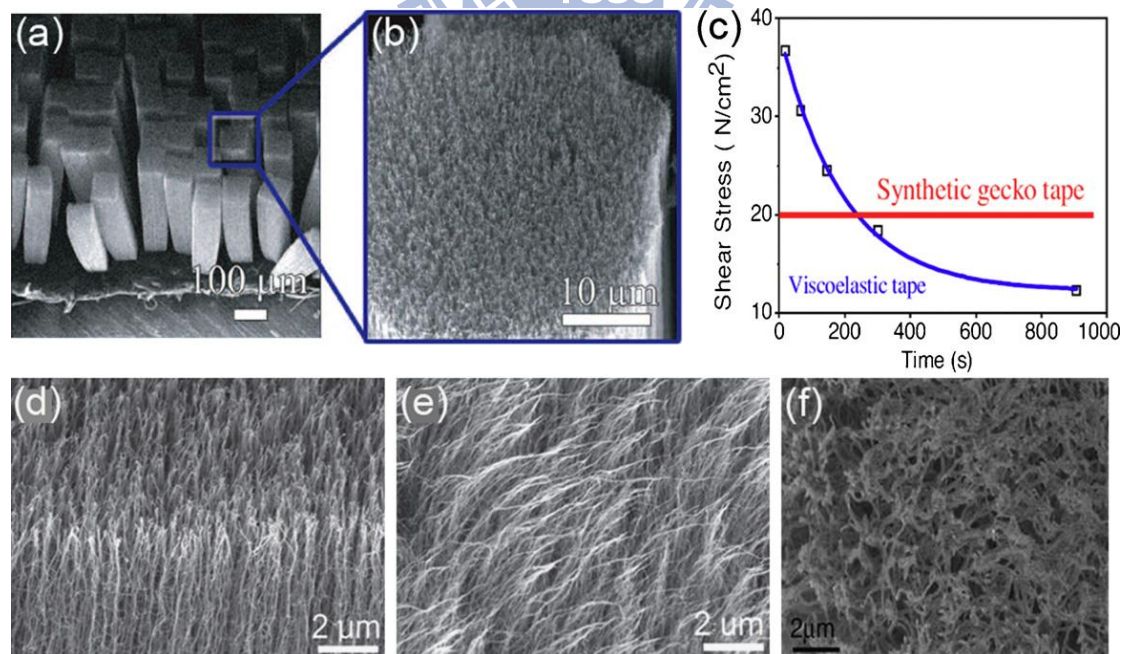
Figure 2.24 SEM images of CNT-based dry adhesives and its durability. (a), (b) Micropatterned CNT arrays by photolithography and chemical vapor deposition and

(c) their durability of adhesion. SEM images of the MWCNT arrays (d) before and (e) after adhesion measurements. (f) Collapsed CNT arrays after applying preload.

2.3.2 Distinctive self cleaning gecko foot

Learning from nature creatures, we can find that nanostructures are essential in fabricating super hydrophobic surfaces with high CA, and multiscale structure can effectively reduce the angle of hysteresis of water droplets.

In general, surfaces with a static CA higher than 150° are defined as super hydrophobic surfaces. As for the details of CA hysteresis [66-68], five states are possible for super hydrophobic surfaces (Fig. 2.25): Wenzel's state, Cassie's state, the so-called "Lotus" state, the transitional state between Wenzel's and Cassie's states, and the "Gecko" state.
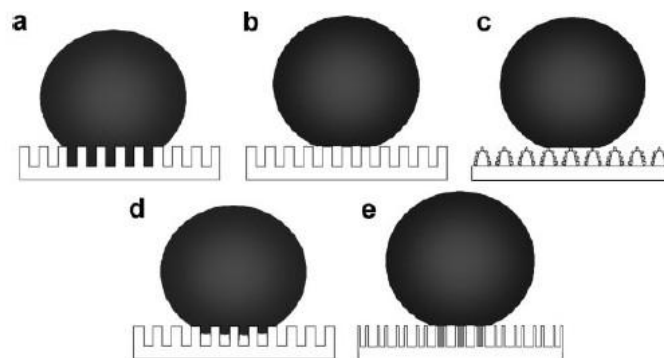
Figure 2.25 Different states of superhydrophobic surfaces: (a) Wenzel's state, (b), Cassie's superhydrophobic state, (c) the "Lotus" state (a special case of Cassie's superhydrophobic state), (d) the transitional superhydrophobic state between Wenzel's and Cassie's states, and (e), the "Gecko" state of the PS nanotube surface. The gray shaded area represents the sealed air, whereas the other air pockets are continuous with the atmosphere (open state).

The phenomenon of self-cleaning in gecko setae is out of general thinking because setae are adhesive and can self-clean when dry. Adhesion in gecko setae is a consequence of many divided contact points (spatulae) that deform to achieve intimate, high-density contact with the surface, whereas lotus-like surfaces remain slippery because their rough, and in some cases waxy, cuticle prevents intimate contact. Lotus-like surfaces require water as a cleaning agent [69-70], whereas self-cleaning in gecko setae may occur because it is energetically favorable for particles to be deposited on the surface rather than remain adhered to the spatula as shown in Fig. 2.26b and c. We can model spatulae as curved surfaces with approximately spherical geometry at the interface, and also work at flexible strips. In each case, we compare the magnitude of attraction between a spherical dirt particle and a planar wall to the combined attraction of the same particle to a number of spatulaeas shown in Fig. 2.26a. This model suggests that > 26 spatulae would need to be attached simultaneously to a single 2.5 μm-radius dirt particle in order for self-cleaning not to occur, assuming similar Hamaker constants (A) and gap distances. Hamaker constants are unlikely to vary by more than a factor of 2; if we take the worst case where $A_{ps} \sim 2A_{pw}$,(where p and w refer to particle and wall, respectively) energetic equivalence occurs with 13 spatulae attached. Gap distance remains an unknown parameter in the model. Until measurements are available, we will assume that D_{pw} and D_{ps} have similar probability distributions, and thus can be assumed to be approximately equal.
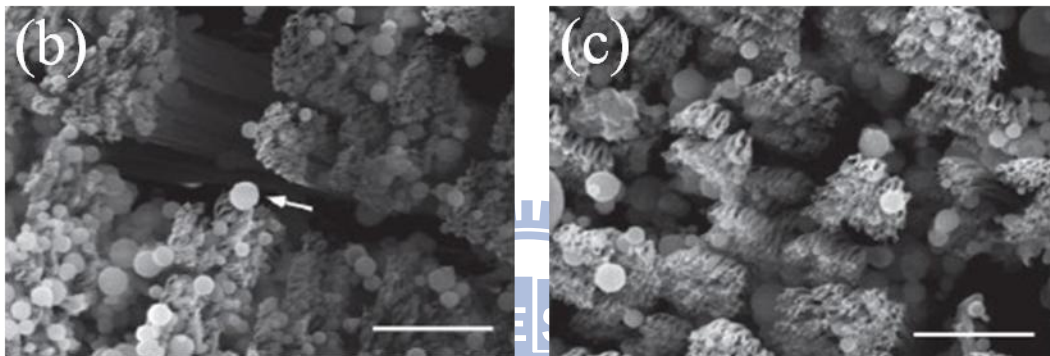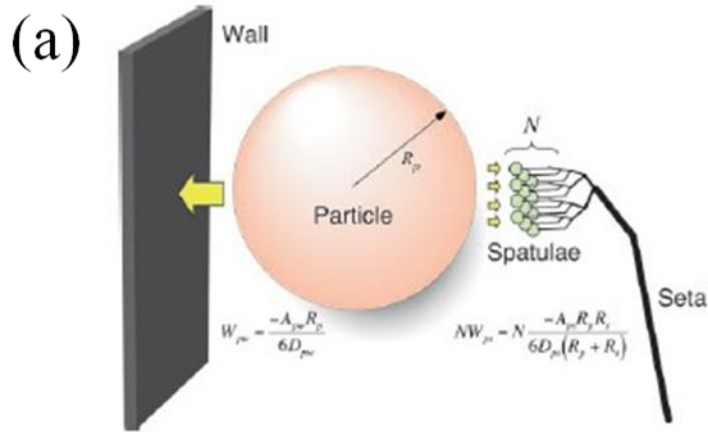
Figure 2.26 (a) Model of interactions between N gecko spatulae of radius Rs, a spherical dirt particle of radius R_p, and a planar wall. Van der Waals interaction energies for the particle-spatula (W_{ps}) and particle-wall (W_{pw}) systems are shown and D is the particle-to-wall distance. Our results suggest that N is sufficiently great that self-cleaning results from energetic disequilibrium between the wall and the relatively few spatulae that can attach to a single particle. (b) Representative array after dirtying with microspheres. Arrow indicates a microsphere adhering to several spatula c, array from the same animal after five simulated steps. Microspheres are still present, but spatular surfaces are mostly clean (Scale bars: 10 μm).

2.3.3 Gecko analysis

Adhesion is the result of attractive forces between two solids with surfaces in close proximity. The opponent of adhesion is the elastic strain energy of the solids as

they deform to optimize their contact. A well-known model that treats this energy balance for two contacting spheres is the Johnson–Kendall–Roberts (JKR) theory [71]. It predicts the force necessary for producing a contact area with radius a between two spherical solids of radius R as

$$F = \frac{4}{3}\frac{E^* a^3}{R} - \sqrt{4\pi E^* \gamma a^3} \quad \cdots \cdots \cdots \cdots \cdots \cdots \cdots \cdots \quad (1)$$

where E* is the Young modulus of the contact pair, and γ is the work of adhesion. The first term in Eq. **1** corresponds to the Hertz solution in the absence of attractive surface forces. The assumption of such forces leads to the prediction of a theoretical pull-off (or adhesion) force between a sphere and a plane given by

$$F_c = \frac{3}{2}\pi R \gamma \quad \cdots \cdots \cdots \cdots \cdots \cdots \cdots \cdots \cdots \cdots \cdots \cdots \quad (2)$$
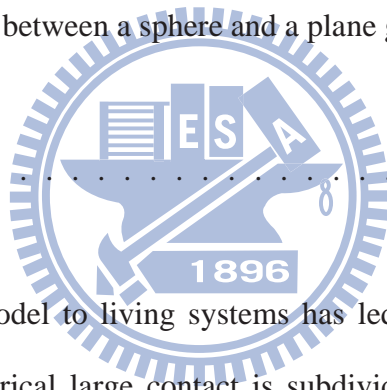
Application of the JKR model to living systems has led to the ''contact splitting'' principle [72]: If one spherical large contact is subdivided into n smaller contacts, with identical apparent contact area, the adhesion force rises by a factor $n^{1/2}$. This principle is reflected in the design of the attachment pads of different natural species. Heavier animals with different lineage (including flies, beetles, spiders, and lizards) display progressively finer contact elements (Fig. 2.28). Assuming that the adhesion force is proportional to body mass, a theoretical dependence of number of contacts versus animal mass has been derived which matches the observed correlation [72]. An additional feature in gecko locomotion is the rapid switching between attached and detached states. Understanding this mechanism is essential for producing responsive adhesives. Recent studies have revealed that geckos move by utilizing both adhesion in the normal direction and friction in the lateral direction [73-74]. These two

components are strongly coupled: the friction enhances the adhesion when geckos grip onto substrate surfaces, called ''frictional adhesion'', while both forces fall to almost zero during detachment with little expenditure of energy by the gecko (''directional adhesion''). This mechanism arises if the fibrils are not vertical, but tilted with respect to the surface. It is because an angled structure significantly lowers the effective modulus of the surface [75]. According to a previous study, the effective modulus should be less than 100 kPa for ensuring a tacky surface (so called ''Dahlquist criterion''), which is given by [75]

$$E_{eff} = \frac{3EID\sin\theta}{L^2\cos^2\theta[1\pm\mu\tan\theta]} \quad\cdots\cdots\cdots\cdots\cdots\cdots\cdots\cdots \quad (3)$$

where E is the elastic modulus, I is the moment of inertia ($\pi R^4/4$, R is the radius of hair), D is the hair density, L is the hair length, μ is the friction coefficient, and θ is the slanted angle. For vertical nanostructures, it is extremely difficult to meet the Dahlquist criterion unless the AR of the structure is extremely high. For example, the AR should be larger than 2×10^2 for the vertical nanohairs with 100nm diameter assuming the slanted angle of 89∘ ($E = 1$GPa, $D = 1.1\times1013$ m^{-2}, $\mu = 0.25$), as shown in Fig. 2.27b [72].
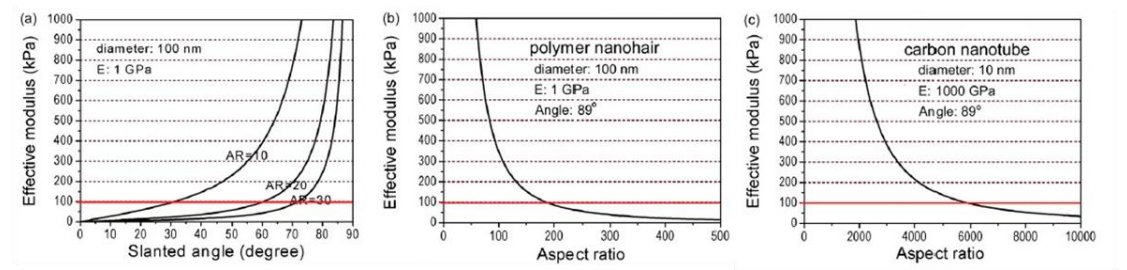
Figure 2.27 Effective modulus of nanohairy structure as a function of (a) slanted angle and (b,c) aspect ratio. For ensuring tacky surface, the effective modulus should become lower than 100 kPa, which meets is the Dahlquist criterion.
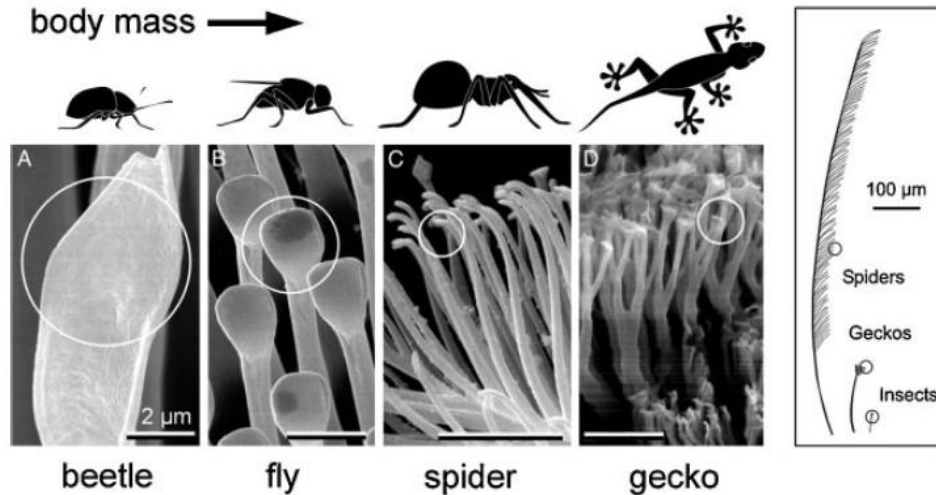
Figure 2.28 Contact tips (circles) in animals with fibrillar design of attachment pads. Note that heavier animals exhibit finer adhesion structures. The scale bar represents 2mm.

This value is not easily achievable using polymeric materials with current fabrication techniques. Even if possible, the self-matting problem or structural buckling will occur due to too high AR and limited modulus of polymers [76-77]. On contrast, if the structures are slanted, the effective modulus can be greatly reduced without the need of structures with extremely high AR. As shown in Fig. 2.27a, for 100nm nanohairs with AR of 20 (E = 1GPa, D = 1.1×1013 m^{-2}, μ = 0.25), the effective modulus decreases less than 100 kPa when the structures are slanted with less than 60° angle with respect to the horizontal plane. Most solid surfaces are not perfectly smooth and have some degree of roughness. Therefore, the height of nanohair should be long enough to ensure adaptation of rough surface with varying amplitude and topography. The maximum height of polymer nanohair (h_{max}), however, is restricted by a critical value that is involved in lateral collapse of hairy structures due to relatively low elastic modulus of polymers. The value of h_{max} for given elastic modulus, size and surface energy of nanohairs is given by [76]

$$h_{\max}(L) = \left(\frac{\pi^4 ER}{2^{11} \gamma_s (1 - \upsilon^2)} \right)^{\frac{1}{12}} \times \left(\frac{12 ER^3 \left(W/2 \right)^2}{\gamma_s} \right)^{\frac{1}{4}} \quad \cdots \cdots \cdots \cdots \cdots \quad (4)$$

where R is the radius of hair, r is the surface energy, W is the distance of two neighboring hairs, E is the elastic modulus of hair, and ν is the Poisson's ratio. According to Eq. **4**, the maximum AR of polymeric nanohairs without self-matting is about 10~20, limiting the absolute height of nanostructures significantly. In this regard, micro/nanoscale combined hierarchical structures could be useful, as they increase adhesion strength against a rough surface either by enhancing structural height or by reducing structural stiffness without structural instability observed in high AR nanostructures [78]. As to the adhesion, the adhesion energy, which consists of the energy dissipated along the interface and the elastic energy stored in the fibril volume, should be concerned without doubt.

$$\gamma_{eff} = \varphi \left(\gamma + \frac{P_{cr}^2}{2E(WH)^2} L \right) \quad \cdots \cdots \cdots \cdots \cdots \cdots \cdots \cdots \cdots \quad (5)$$

where L is the length of the fibrils, P_{cr} is the critical force required to peel an elastic thin film off a rigid surface, W is the width of the film, H is the thickness of the film and φ is the area fraction of the fibril array. According to Eq. **5** [78-79], the larger the length of the fibrils are, the higher will be the adhesion energy. Taking L = 120 μm as the length of a seta, we can find $\gamma_e \gg \gamma$. For φ~1, when the peeling angle of the spatula pad is $\theta = \pi/2$, we have $\gamma_e = 10$ J and $\gamma = 0.1$ J; when the peeling angle of the spatula pad is slightly smaller than $\theta = \pi/6$, we find $\gamma_e = 924$ J and $\gamma = 9.24$ J. Therefore, extending the spatula pads to the length of the seta gives rise to a structural unit with much higher adhesion energy than the van der Waals interaction energy. The

increase in adhesion energy is tremendous. At the same time, the effect of orientation dependent adhesion energy for peeling at different angles is magnified through the term P_{cr}^2 in Eq. **5**. Thus, at the scale of the seta, the adhesion energy for attachment is almost two orders of magnitude higher than that for detachment.

2.4 Motivation

Adhesive are used in many aspects of the daily life. In general, such man-made adhesives have high (sometimes extremely strong) adhesion strength but are not easily detached. Furthermore, they are seldom reusable because the surfaces are quickly contaminated by adhering materials due to their tacky feature. In contrast, nature has created its own adhesives with unique structures and functions. Dry adhesion mechanism in gecko lizards has attracted much attention as an excellent example, because it provides strong, yet reversible attachment against surfaces of varying roughness and orientation. Theoretical and experimental investigations into the field of mimicking gecko adhesives are very numerous; however, they cannot take all advantages of gecko due to materials' limitation compared with nature material from gecko. Moreover, they need an expensive and sophisticated process, limiting widespread uses of the methods. Especially for the hierarchy structure, which can offer a much more stable and stronger adhesion, is hardly fabricated. This study designs the efficient method of an innovate structure to improve a stronger and more stable adhesive than other approaches. Besides, without losing any adhesion force, self-cleaning surface can also be obtained via these tapered shaped pillars in such a specific size. We are riding the decade's giddiest train of technology, revealing human want multi-function products instead single feature product. The proposed model of taper shaped pillars adhesives may prompt application in any others gecko-mimicking adhesives. We believe such a novel structure which is a low-cost, brilliant adhesion; highly stable and even self-cleaning is integral and promising for the future using.

Chapter 3: Experiments

3.1 General Introduction

All the experiments were preceded in National Chiao Tung University (NCTU). All the equipments were also conducted in our laboratories in NCTU. The reagents were purchased commercially and used by following with the directions unless specially mentioned.

All the reagents were listed alphabetically in the form of "Name {abbreviation; chemical formula; purity; manufacturer}". Some information will be omitted if not available or not necessary. The following text will use the abbreviation of the reagent.

Deionized and distilled water {DI water, ddH2O}

The water we used was purified with filters, reverse osmosis, and deionized system until the resistance was more than 18 $M\Omega \cdot cm^{-1}$. DI water was used to clean, wash, and be a solvent.

Aluminum foil {99.999%; ADMAT}

Aluminum foil was used for fabricating AAO in a two-step process.

Phosphoric acid {H₃PO₄; 2.5%; J.T.Baker}

In general, the diameter of AAO was decided by the electrolyte used and voltage applied, so that we choose phosphoric acid to get the AAO with 350 nm diameter for our template at HA conditions.

Oxalic acid dehydrate {H₂C₂O₄; 99.8%; J.T.Baker}

In general, the diameter of AAO was decided by the electrolyte and applied voltage, so that we choose oxalic acid to get the tapered AAO with 70 nm in diameter for our template at HA conditions.

Phosphoric acid {H₃PO₄; 5%; J.T.Baker}

Phosphoric acid in 5% is essential for our AAO porous structure to remove the alumina film and expand the pores.

Ethanol {C$_2$H$_5$OH}

In this study, it was used for washing and part of electrolyte for low temperature method.

Polydimethylsiloxane {PDMS (Sylgard 184); Dow Corning}

We used PDMS to support h-PDMS in case of breaking.

1H,1H,2H,2H-perfluorooctyltrichlorosilane{C$_8$H$_4$Cl$_3$F$_{13}$Si; 97%; Alfa}

In this study, it was regarded as a anti-sticking layer to reduce surface energy.

Polyurethteneacrylate{soft PUA; Minute Tech}

We used PUA for the replication and our artificial adhesives.

3.2 Experimental Methods

AAO Template Fabrication

Aluminum plate

↓ Clean

Electropolishing

↓

Two-step HA procedure

↓

Fabricating tapered hole by HA in $C_2H_2O_4$

↓

Tapered AAO Template

AAO Template

↓

Anti-sticking coating

↓

Directional replication ← [**PDMS** **h-PDMS** **PUA**]

↓

Tilted curing

↓

Tapered shape pillar

↓
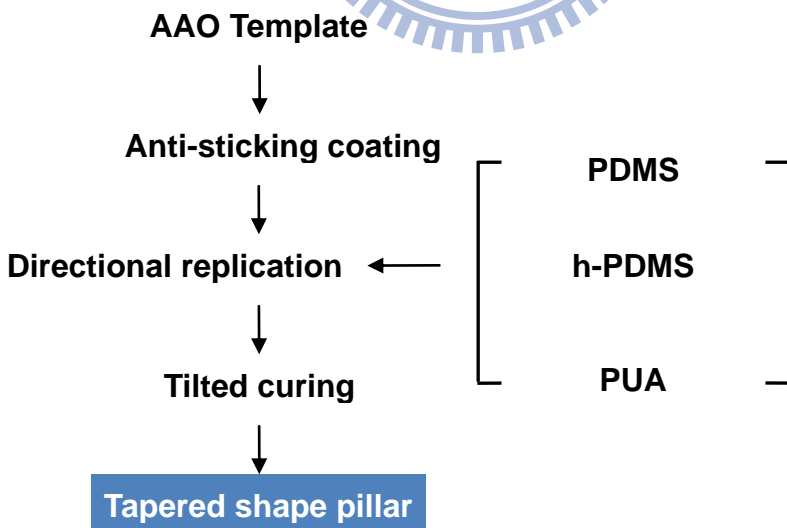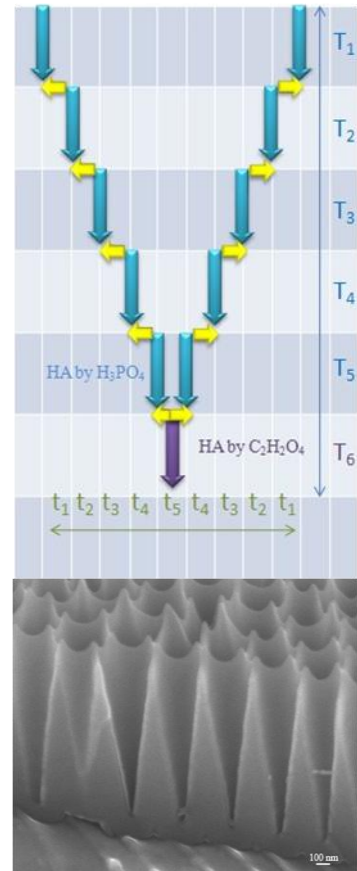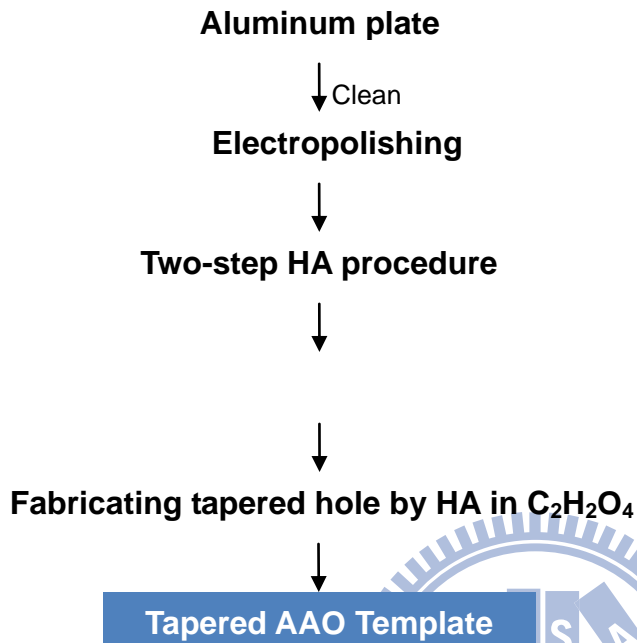
- **SEM**
- **Adhesion measurement**
- **Self cleaning property measurement**

Figure 3.1 Experimental flowchart for the fabrication and analysis was divided into two parts including AAO template (upper) and tapered shape pillar structure (lower). Following SEM images by side shows the morphology.

3.2.1 Preparation of Porous Anodic Alumina

Square aluminum foils (99.999% purity) with 3 cm edge were degreased in acetone, washed in de-ionized water, and put into a tailor-made holder with an opening of 3 cm^2. Before anodizing, the aluminum was treated with annealing at 450°C for 12 hr and electropolished at a constant voltage in a 1:4 volume mixture of perchloric acid and ethanol under room temperature. The $C_2H_2O_4$–C_2H_5OH–H_2O electrolytes, and H_3PO_4–C_2H_5OH–H_2O electrolytes are designated as S1 and S2, respectively. For the pre-step HA, the concentrations of phosphoric acid in the electrolytes were in the range of 0.25 M. The temperatures of the electrolytes were kept at −10°C by a powerful low-constant-temperature bath, and samples were anodized at target voltages 195 V for 10 min. After the selective removal of alumina in a mixture solution of CrO_3 and H_3PO_4, the first HA was carried out under the same anodization conditions. During the first anodization step, the shape of the holes was precisely controlled by changing the times of anodization and etching in phosphoric acid at 53°C as shown in Fig. 3.2. For the second step HA, the concentrations of oxalic acid in the electrolytes were in the range of 0.1M, the temperatures of the electrolytes were kept at -10 °C, samples were anodized at target voltages 195 V for 10 s, the PAA template with pore diameter of 380 nm and length of 1.3 μm was obtained.

Fig. 3.3 shows the schematic diagram of experimental setup for the aluminum electropolishing and anodization. A specially designed one-electrode cylindrical cell double layer glass cup was used which can let cooling water flow through. The anode

was the aluminum film specimen and a graphite flake was used as the cathode. Because edges of the aluminum plate undergoing stronger electric field have a faster reaction rate than center, only a part of the film was exposed to the electrolyte through an open circle with an area of about 1.5 cm^2 on the cylinder, and there was an O-ring clipped between the specimen and the tank fixed by a jig. GW laboratory power supply (model GPC-3060D) was used as the anodizing source.
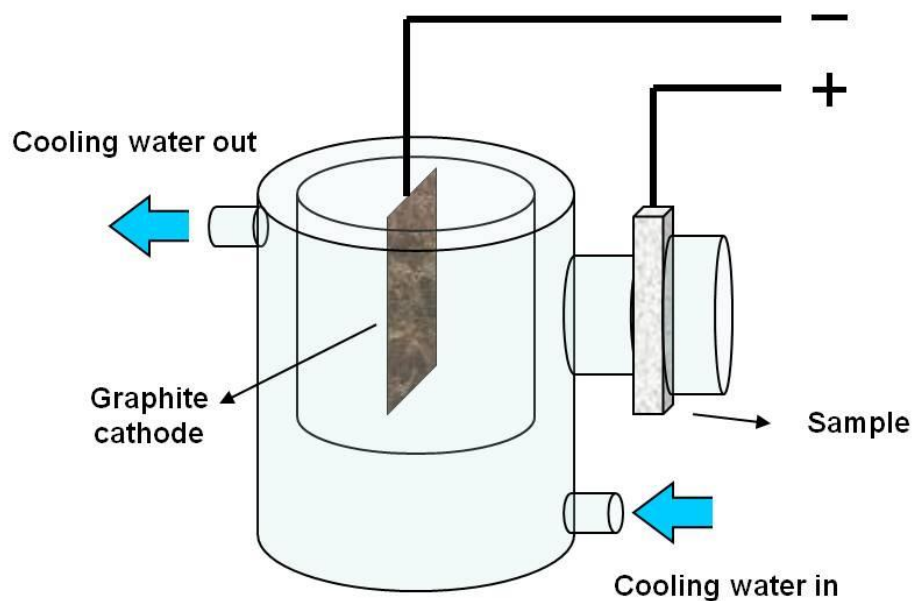
Figure 3.2 The schematic diagram of experimental setup for the aluminum electropolishing and anodization.

3.2.2 Nondestructive replication of master mold and method of slanted structure

The taper shaped gecko-like structure via self-ordered porous alumina hard templates serving as shape-defining molds is well-established. After preparing the tapered AAO master with a specific feature size, we fabricated tapered nanohairs by replicating the master with soft UV-curable polyurethane acrylate (PUA) and

thermalplastic h-PDMS in different process, respectively, shown in Fig. 3.4. The master was treated with a fluorinated SAM solution (FOTCS, Gelest Corp.). The treated master mold was annealed at 120 ^{0}C for 20 min. Drops of soft PUA (301RM, Minuta Tech.) prepolymers were dispensed onto the master mold and UV-transparent able silica was slightly pressed against the liquid drop as a supporting backplane. After preparing a polymer replica by UV exposure for 1hr through the tranparant back side (dose = 15 mJ/cm^2) and mold removal, the PUA replica was additionally exposed to UV for 10 h for complete curing.
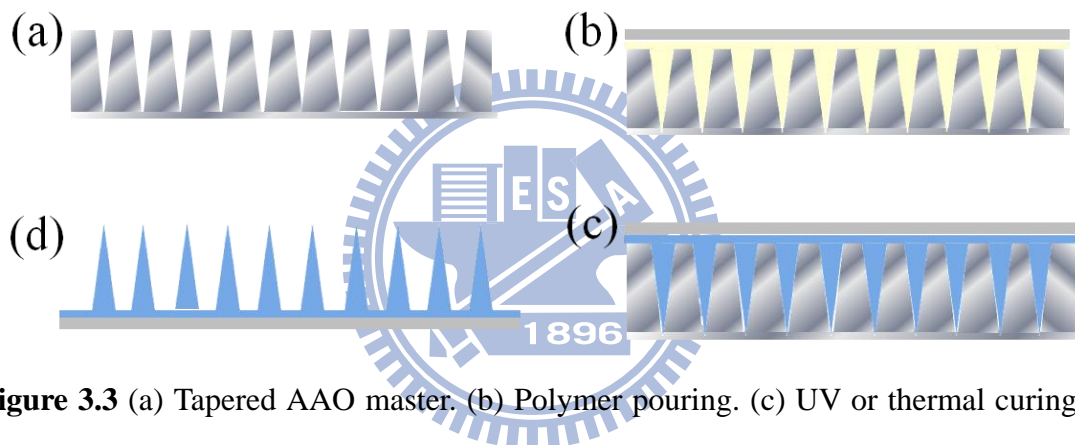
Figure 3.3 (a) Tapered AAO master. (b) Polymer pouring. (c) UV or thermal curing, and (d) peel off from master.

As to the slanted structure in our experiment, we conceive a brand new methods inspired by our experiment data. Fig. 3.4 shows the SEM image of the exposed taper shaped pillar after pressing by carbon tapes. The results urge me to use this skill for a ordering slanted sturcture. We can esily find the optimal parameters including the pressure, curing and press time to fabricate the ordering tapes.
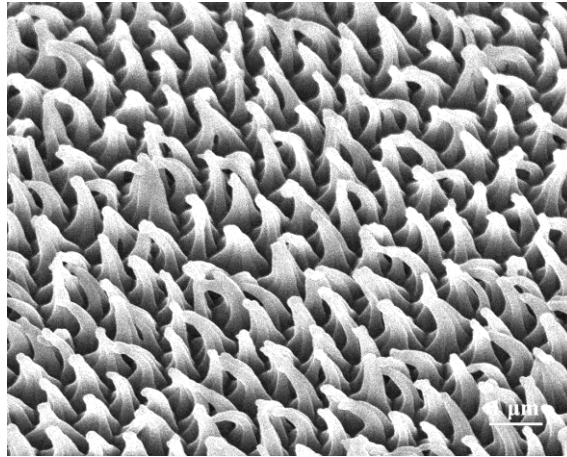
Figure 3.4 SEM image of the exposured taper shaped pillar after pressing by carbon tapes.

3.2.3 Assaying the Specimen

SEM

SEM is a very useful tool for observing surface morphology of specimen. The morphology of the Al_2O_3 pore arrays were all characterized by a field-emission scanning electron microscopy (FE-SEM, JEOL-6700) operating at 10 k eV accelerating voltage.

3.2.4 Dry adhesive force measurement and repeating cycle on silica

Counter weight equipment

The gripping and releasing force was measured via counter weight and preload force which means the force during the attachment.

Forward direction   *Reverse direction*
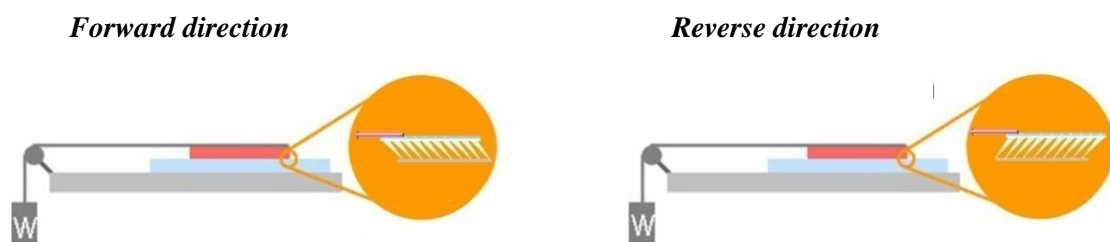
3.2.5 Self-Cleaning property measurement

Contact angle meter

A measurement of a static contact angle is a general method to understand the wetting phenomena of a surface. A surface with a static contact angle larger than 150 degree is regard as a super hydrophobic surface. Herein, we investigated the anti-wetting properties of the resulting surfaces by using a contact angle meter (FTA175). The average contact angle was from five different position measurements on the same surface.

Chapter 4: Results and Discussion

4.1 Control Factors of Fabrication of Anodic Alumina Oxide

HA (hard anodization), which is highly dependent on current density and temperature, is utilized to fabricate taper AAO in our work. Fig.4.1 presents the SEM images of taper AAO with 1.3 μm in length and 380 nm in diameter. HA and MA (mild anodization) are quite different in current density, film growth rate and interpore distance (D_{int}) as shown in Table 4.1. From Fig. 4.2, unlike the typical anodization curve for MA, the current density in HA shows a nearly exponential decrease as a function of time which have been reported in detail [1]. Larger current density caused by larger voltage (Fig. 4.2) will lead to a high growth rate due to the extremely rapid movement of ionic species (O^2, OH, Al^{3+}). Film growth rate is highly dependent on current densities, once a given value of current density can stand for a corresponded growth rate through our database. Fig. 4.3 showed AAOs of different lengths via the same film growth rate, which is related to the current densities of HA, in different processing time. Furthermore, high anodizing current density will induce a denser penetration path distribution during the initial stages of film growth compared with MA. The repulsive interaction force between the alumina cells (from high current density) limited the transverse growth of alumina cells and force them to form close-packed hexagonal arrays, thus producing highly ordered AAO quicker than MA as shown in Fig. 4.1c, d.
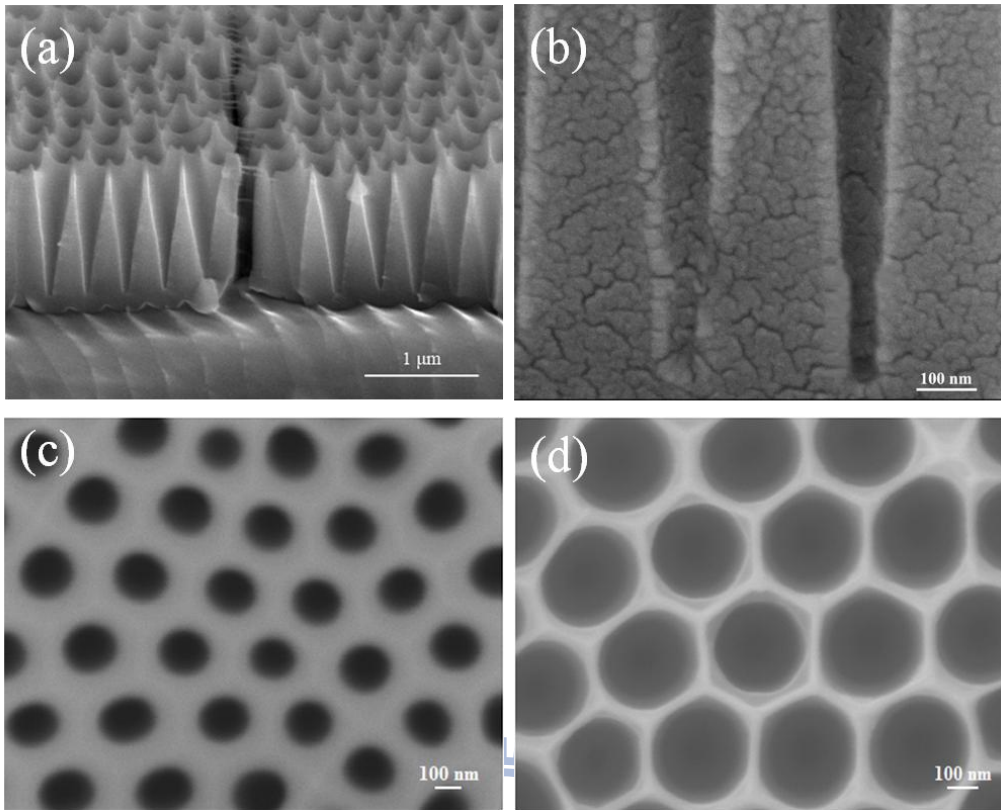
Figure 4.1 SEM image of our taper shape AAO. (a) From cross section (1.4 μm). (b) Fine structure. (c) From top view with less pore widening. (d) From top view with more pore widening (380 nm).
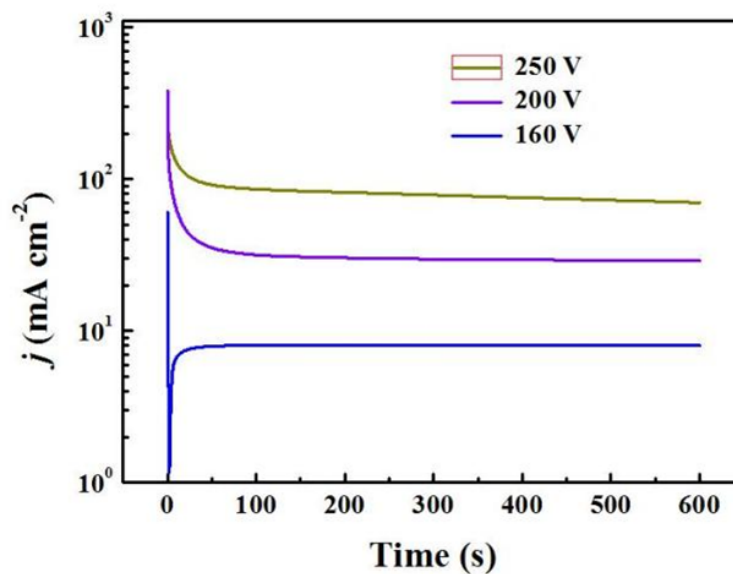
Figure 4.2 Current versus time during HA in 0.25M H_3PO_4 (-10^0C). A conventional MA (0.25M H_3PO_4, 160V) is also plotted (blue line) for comparison.

53

	MA	HA
Voltage(V)	160v	Above 190
Current density(mA cm-2)	3	Above 20
Film growth rate(μm h-1)	10	Above 60
Interpore distance(D_{int} ; nm)	405	380
Pore diameter(Dp; nm)	70	90
AAO fabrication is highly dependent On the material and environment		

Table 4.1 MA versus HA in 2.5% H_3PO_4 (-10 ^{0}C).
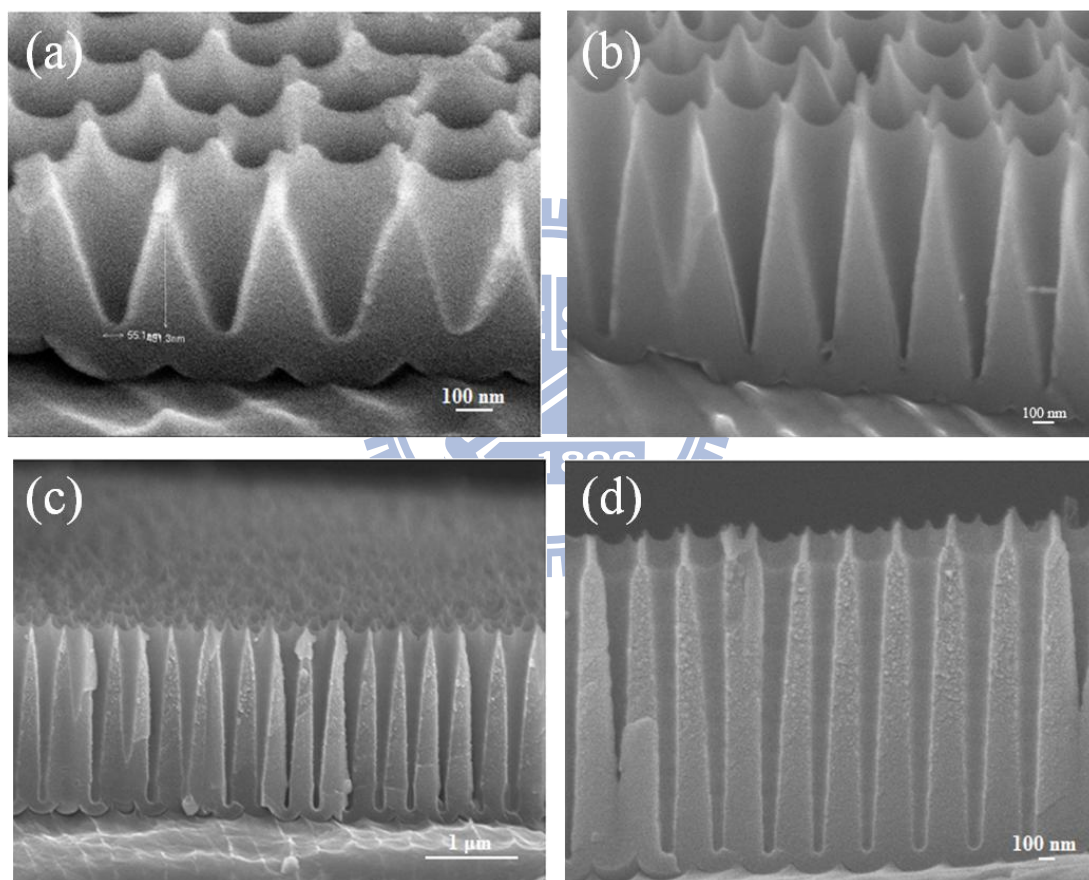
Figure 4.3 SEM images of taper AAO with different lengths. (a) 600 nm. (b) 1.1 μm. (c) 1.8 μm and (d) 2.3 μm.

During the taper AAO fabricating process, we have found few special phenomena such as concentration effect, diameter saturation and decoupling anodization of HA. We discussed the results of these three aspects respectively as

follows.

First, instead of affecting diameter or others, we noted that the concentration only affect the current density which is referred to the ordering and film growth rate. Current density was produced by the movement of ionic species which acquire more in higher concentration electrolyte. On contrast, however, large current density may also cause the joule heat which will destroy the ordering and bring about unstable situation. Once the cooling system cannot release the tremendous heat instantly, the orientation will be disturbed. We discovered that the optimal concentration is 2.5% for producing and releasing heat from the sample best as shown in Fig. 4.4d. According to Fig.4.4a, 1% H_3PO_4 solution cannot afford enough ionic species, but 10% H_3PO_4 solution provided excessive ionic species and joule heat to obtain high ordering.
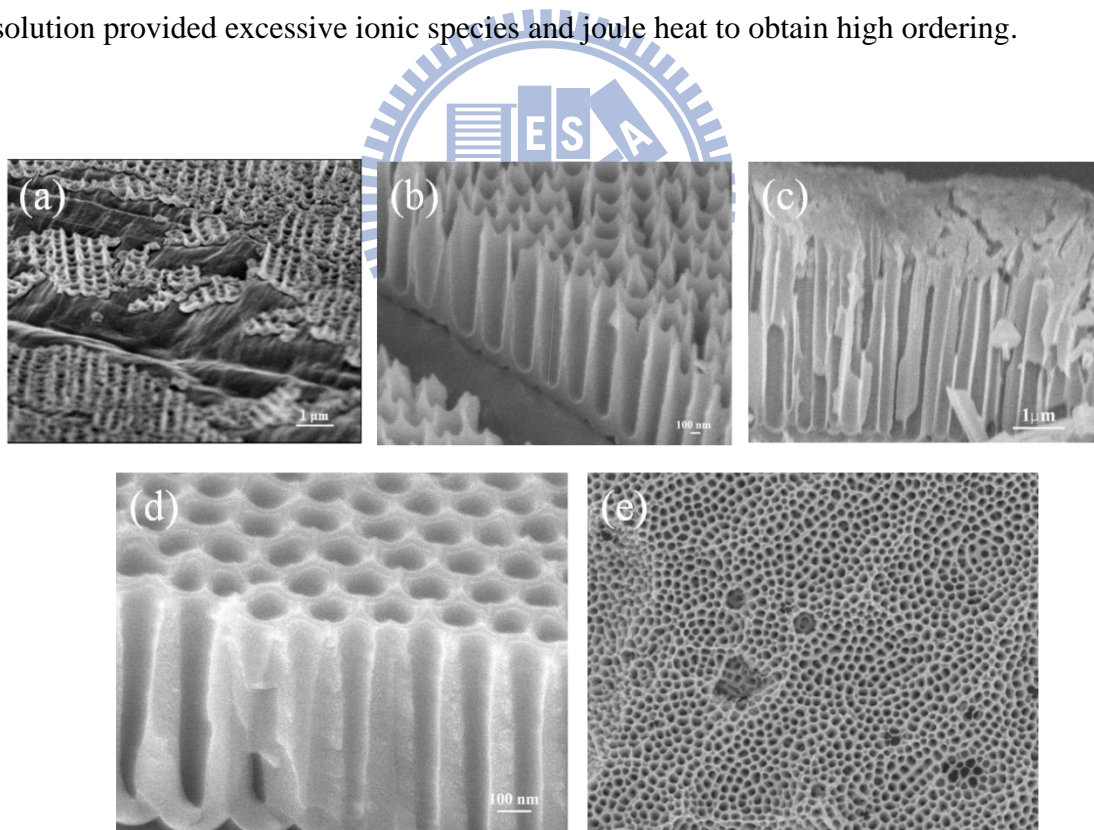
Figure 4.4 Processing anodization in phosphoric acid with different concentration. (a) 1% which cannot offer enough ionic species. (b) 5% (c) 10% with excess jeoul heat from current densities. (d) 2.5% and (e) top view of AAO in 10% concentration.

Second, the ordinary empirical relationship between voltages and diameters of AAO are D_{int} = 2.5 Ea for MA and D_{int} = 2 Ea for HA. The linearly relationship will vanish above a saturation value of voltage, and left the better ordering arrangement with increasing current density, which is induced from large voltage (Fig. 4.5). The strong repulsive force between the alumina cells induced by higher current density may be the main reason of the saturate diameter. . That is, we can acquire a highly ordered AAO with increasing voltage as long as the joule heat induced from current density can be released by the powerful cooling system (Fig. 4.5e).
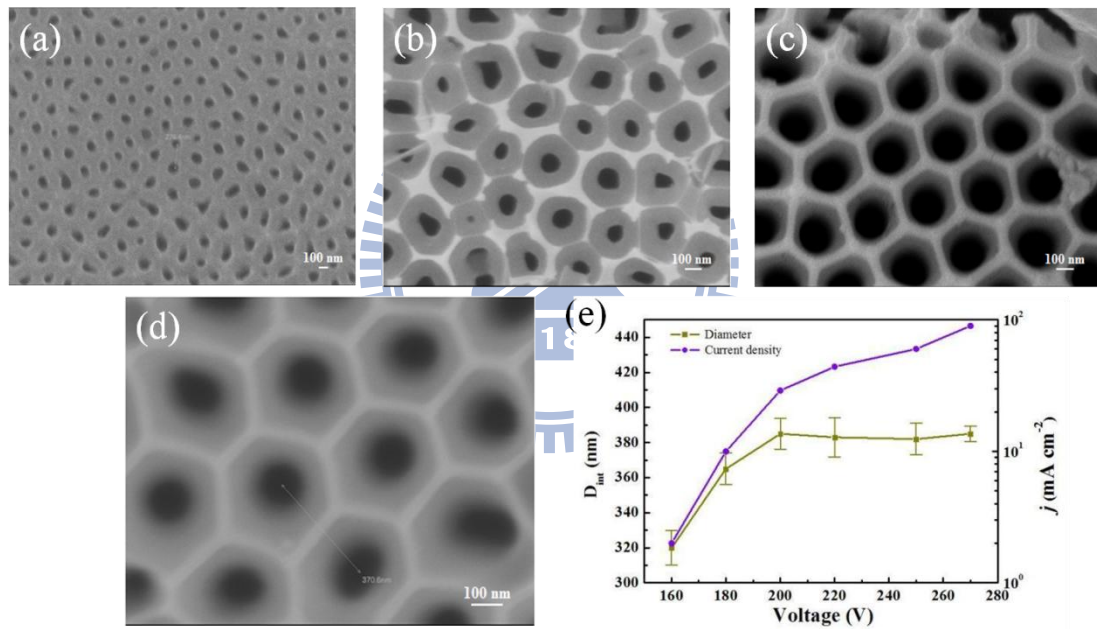
Figure 4.5 (a) to (d) Demonstrate that as voltage parameter increases, the ordered condition increases. (e) Relationship between interpore distances, current densities and voltage.

Finally, we also perceived the decoupling system through using different electrolyte in HA can support us to modulate nanopore diameter with different porosity, hence resulted in the fine structure which facilitated the adhesion force of

PUA as shown in Fig. 4.1b and Fig. 4.6. Conventional two-step anodization process should be done with the same electrolyte and voltage in both steps which will also cause the same porosity in both steps. With our two-step decoupling anodization, the pore size and interpore spacing of ordered AAO can be independently controlled without using expensive and cumbersome imprinting. For instance, we could fabricate the second step in oxalic with same voltage as the first step (in phosphoric acid) and resulted in a smaller pore diameter about 60 nm. The ratio of D_{int} to Ea is 2 ($D_{int} = 2$ Ea) for both phosphoric acid and oxalic in HA. Fig. 4.6c and d present the fabrication of AAO beyond the processing windows (with different voltage in each step) conduce to a breakdown of ordering.
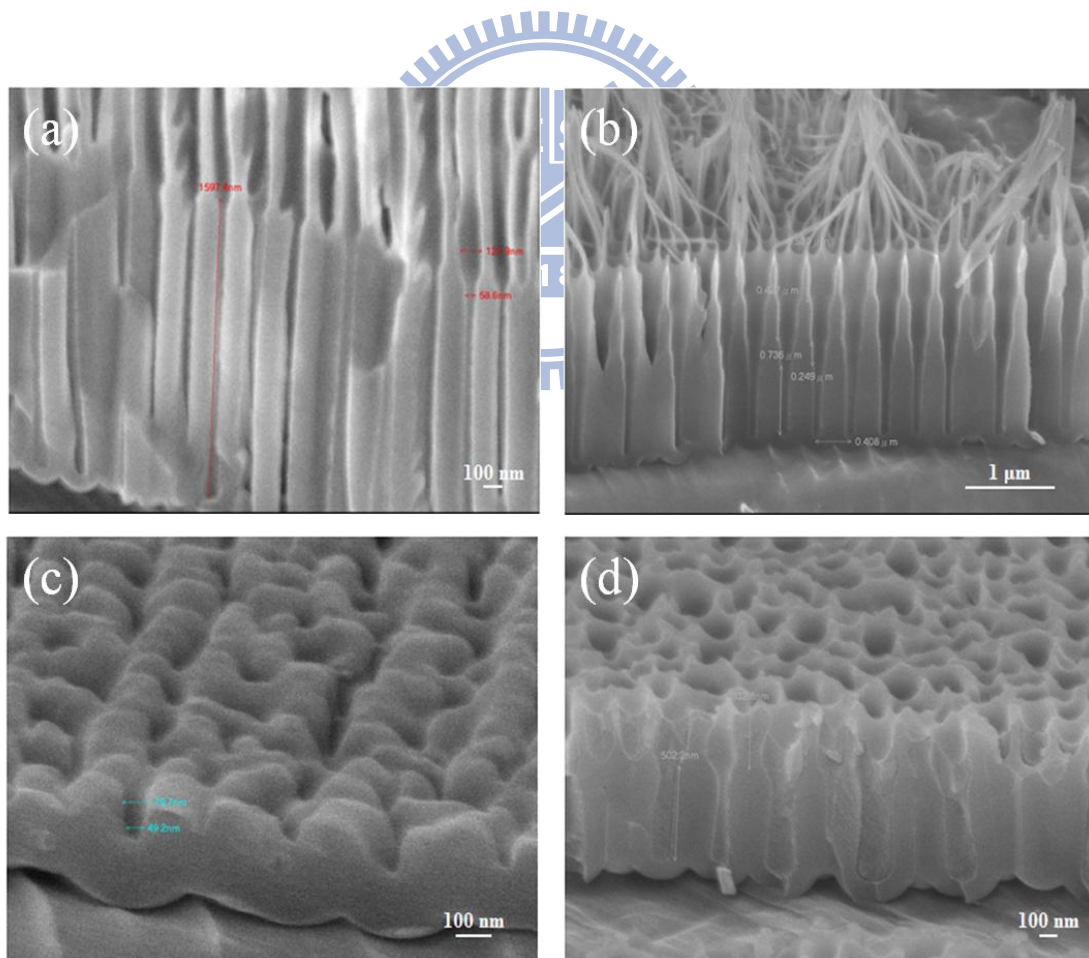
Figure 4.6 SEM images of decoupling system. (a,b) Optimal processing widows in both first and second step. (c) Unmatched voltage cause a bad result because the

57

applied voltage at second step is too small and (d) too big to fit the optimal condition.

To sum up, using phosphoric acid as an electrolyte required a higher working voltage and current density to obtain ideal interpore distance ,hence it will be harder to fabricate AAO compared with other acid. Without expensive imprinting process, we firstly manufacture highly ordered taper and decoupling structured AAO in phosphoric acid through HA process. Moreover, HA process provided a short anodizing time which avoided disorder structure due to the amassment of joule heat.

4.2 Dry adhesive

In this section, we presented nano-scaled, taper hairy adhesives which can perform high adhesion, high stability and also self-cleaning properties. Getting the vindication from nature animals, we suggest that it is integral for generating high adhesives, which can sustain grant weight such as human being, via nano-scaled structure instead of micro-structure due to an important consequence of contact splitting theory. Our design principle for the nano-scaled taper hairy adhesives is based on this finding. We'll discuss the results, length effect, and the reason of utilizing taper shape, slanted angle for easily releasing and self-cleaning feature as following. Table 4.2 presents the comparison of the gecko mimicking adhesives including our work.

	Gecko foot hair (β-keratin-2GPa) [2]	Slanted taper (PUA) from our work	Angled pillar (PUA - 19.8MPa) [3]	Slanted structure (PP-1GPa) [4]	Pillar structure (h-PDMS-11MPa) [5]	Hierchical structure (PDMS-1.8MPa) [6]	Angled spatulate tip (PU-3MPa) [7]
Fabrication method	Nature	Molding via AAO, pressure tech	Molding and e-beam exposure	Molding	Molding via AAO	Two-step photolithography and soft molding	Two-step photolithography and press tech
Shear adhesion (N/cm^2)	10	8	11	4.5	0.048	2	10
Durability	>30000	>100	NI	NI	NI	NI	>100
Directional adhesion	Yes	Yes	Yes	Yes	No	No	Yes
Self cleaning	Excellent work via steps	Workable via steps and water	NI	NI	High contact angle	NI	NI

Table 4.2 Polymer-based gecko artificial adhesives comparison. (NI = No information)

4.2.1 Design of taper shape

Young's modulus is a fairly important parameter for us to forecast the adhesive ability and whether the hairy structures bunch themselves or not. Conventional adhesives, such as those used in adhesive tapes, must be soft enough. It means that low Young's modulus materials (E < 100 kPa) were used for satisfying Dahlquist's criterion to inherit intimate and continuous surface contact [8]. Definitely, the Young's modulous will vary by the deformation and geometry to fit the criterion as shown in Fig. 2.27. Facile fabrication of high-AR and taper nanostructures by replica molding requires the optimization of mechanical properties of a structured material. If the material is too soft (such as polydimethylsiloxane so called PDMS, with a Young's modulus of 1.8 MPa), the resulting high-AR nanostructure is prone to clump and collapse after molding which will reduce the real area of contact between the adhesive and surface. In contrast, if the material is too stiff (such as carbon nanotube), the

high-AR nanostructure can readily be fabricated, despite a high preloading force and a significant reduction in the adaptability for a rough surface are still the major concern. Hence, the material we using is sufficiently rigid for high-AR replica molding with its modulus 19.8 MPa but low preloading force.

In short summary, in theory, smaller features will generate higher levels of adhesion, and such materials with a higher modulus of elasticity will resist clumping and fouling.

The taper shape is beneficial for its "longer length", "higher stability", "higher adhesion" and better "self-cleaning" ability compared with other shapes, showing the profile and SEM image of taper pillars in Fig. 4.7a, c. Pillars cannot survive at the same conditions of density and length compared with taper shape pillar, that is, the life time or cycles can be improved without additional deposition such as Pt compared with other shapes of nanohairs as shown in Fig. 4.8. Eq. **6** [9] and Eq. **7** [11-12] explain the maximum height of polymer nanohair (H) and the adhesion energy of the fibrils, respectively.

$$h_{\max}(L) = \left(\frac{\pi^4 ER}{2^{11} \gamma_s (1-\upsilon^2)} \right)^{\frac{1}{12}} \times \left(\frac{12ER^3 \left(W/2 \right)^2}{\gamma_s} \right)^{\frac{1}{4}} \dots \dots \dots \dots \quad (\,6\,)$$

where R is the radius of hair, r_s is the surface energy, W is the distance of 2 neighboring hairs, E is the elastic modulus of hair, and ν is the Poisson's ratio.

$$\gamma_{eff} = \varphi \left(\gamma + \frac{P_{cr}^{\;2}}{2E(WH)^2} L \right) \dots \dots \dots \dots \dots \dots \dots \dots \quad (\,7\,)$$

where L is the length of the fibrils, P_{cr} is the critical force required to peel an elastic thin film off a rigid surface, W is the width of the film, H is the thickness of the film and φ is the area fraction of the fibril array.
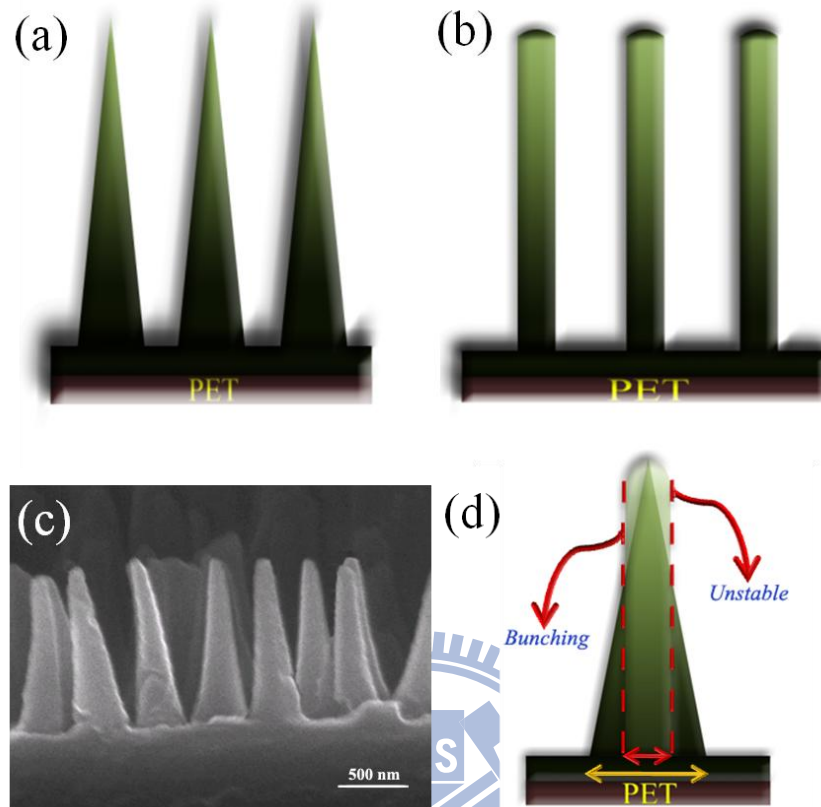
Figure 4.7 (a) Taper shaped pillars profile sketch map. (b) Pillar shape profile sketch map. (c) SEM image of taper shaped pillars and (d) illustration of taper's advantage.
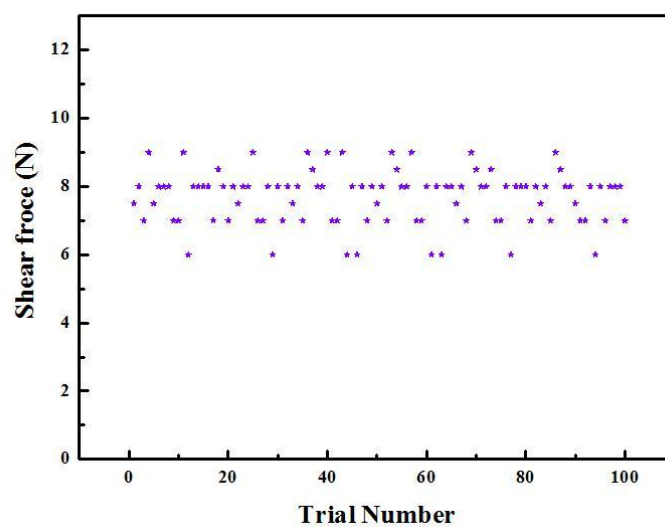
Figure 4.8 Force measurements versus cycles of attachment and detachment, and the force remained the same for over hundreds of time.

According to Eq. **7**, the larger the density (area fraction) or length of the fibrils, which means the high-AR fibrils accompany the high adhesion energy. Taper shape has the advantages compared with pillar shape in both of density and length. The advantage is showing here via this equation, the taper shaped pillar can keep high density of fibrils which referred to adhesion ability while length increasing. Because if the pillar shape reach the same optimal length level as taper shaped pillar, the space between only pillar shapes should be widen in case of bunching, that is, density and area fraction must be decreased dramatically which reduce the adhesion force. Consequently, taper pillar has a better performance than others. Gradient diameter of taper shaped pillar can firmly support whole weight from bottom, and avoids bunching due to wider interval from top. Evidently, taper shaped pillar can did increase the pillar height compared to pillar shape in the same material as shown in Fig. 4.7d. It is also noted that the maximum height of taper shaped and pillar shaped nanohairs in Eq. **6** are in the range of 1.3~1.8 μm and 0.7~1.2 μm (γ_s ~ 40 mJ/m^2 and $v = 0.5$), respectively, corresponding to the height of taper shaped hairs presented here (~1.4 μm and 800 nm). As shown in Fig. 4.9 and Fig. 4.10, different lengths and profiles are fabricated by replicating, and the optimal lengths are 1.4 μm and 800 nm, respectively, which are both fit to the theoretic value.
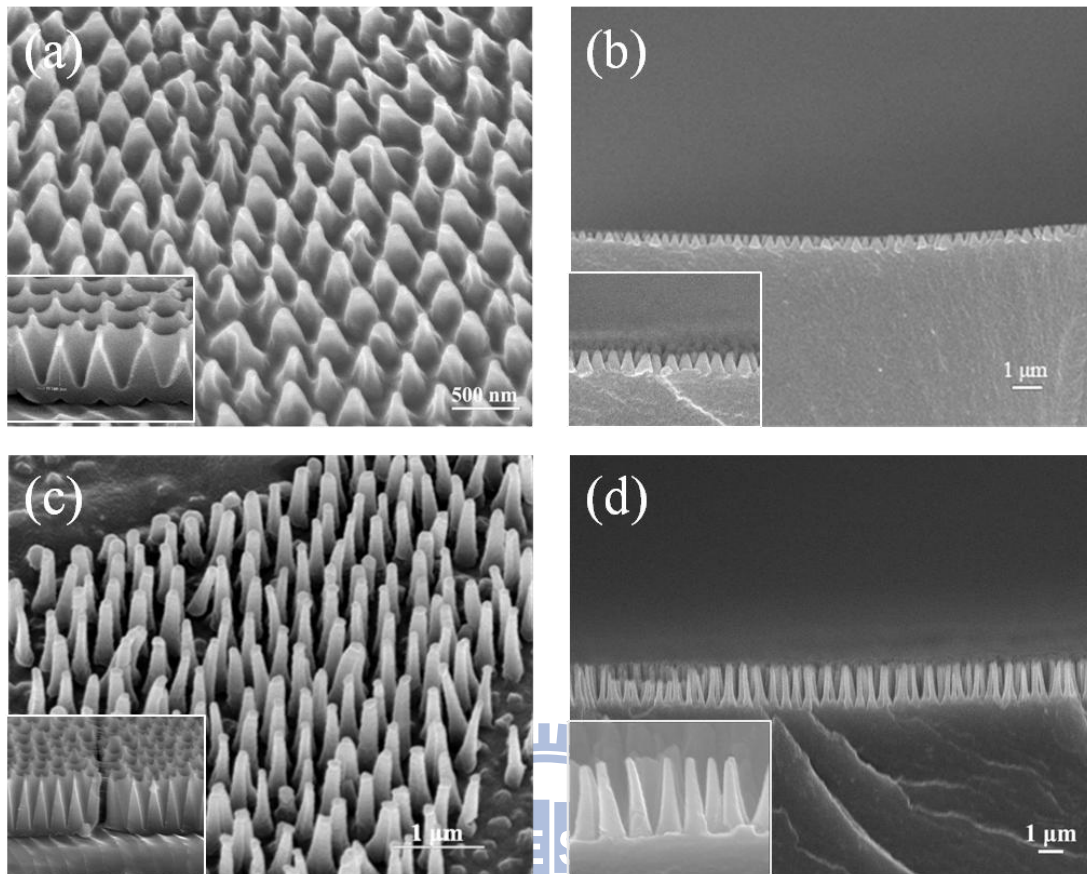
Figure 4.9 Taper pillars with different lengths. (a) 600 nm from tilted SEM image (b) 600 nm from cross SEM image. (c) 1.4 µm from cross SEM image. (d) 1.4 µm from cross SEM image. The insets showed the molds of replicating or SEM images of high magnification, respectively.
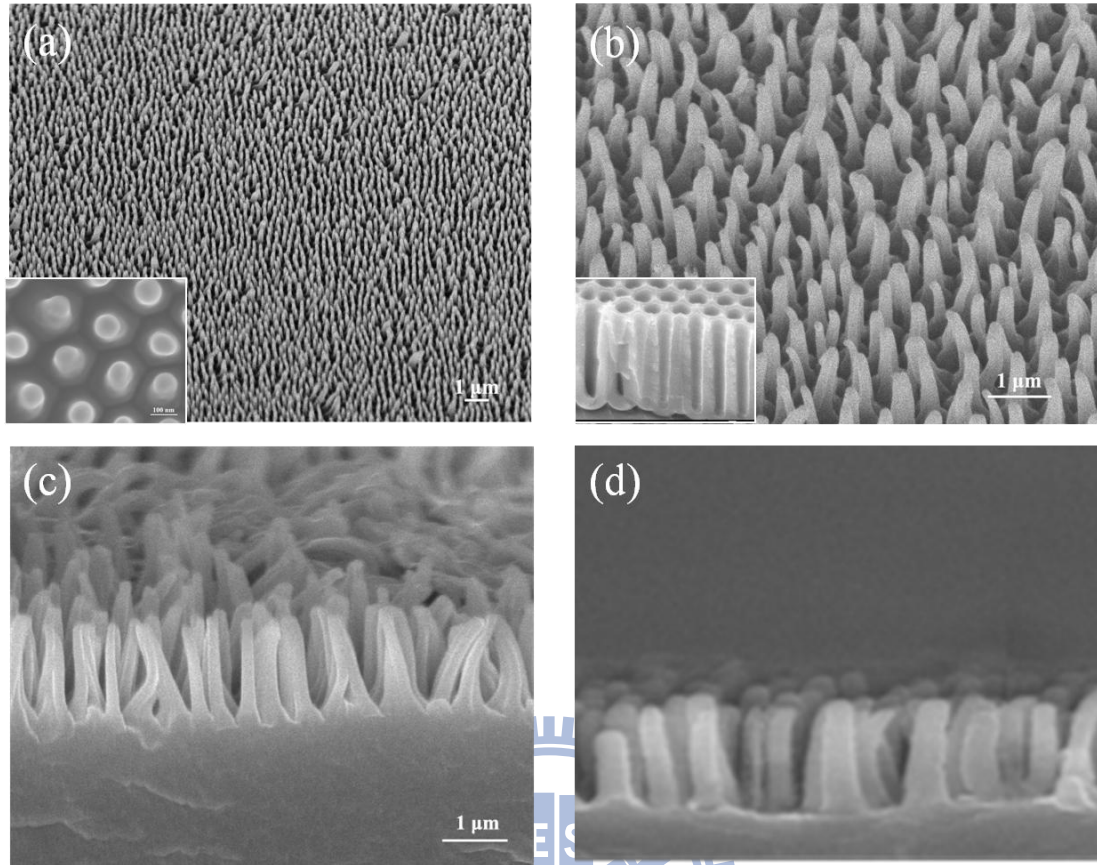
Figure 4.10 SEM images of taper and pillar nanohairs. (a) Low magnification of our structure, and the inset is the top view image that displays the taper edge and hexagonal arrays. (b) Tilted SEM image of the pillar shape showing this type cannot support the same height as the taper shape and (c) SEM image from cross. (d) Stable pillar with decreasing the length.

Gecko's adhesive system is massively reusable and stable because of its multilevel hierarchy that distributes the load and generates such high levels of adhesion because of the smaller features (Fig. 4.11a) [8]. We can easily understand that taper shape could achieve stable and reusable than others due to the gradient diameter from bottom to top of the pillar. The larger diameter at bottom can support longer length and offer a better fundamental base of the pillar in case of breaking by external force, and smaller diameter at top is responsible for higher contact area

related to the adhesion and also avoids clumping which we discussed previously (Fig. 4.7d). We can split the taper shape into several layers staked up one by one as shown in Fig. 4.11b. Moreover, each layer can regard as a sum of hundreds of thousands pillars to support the layer above themselves that is just like the gecko's multilevel hierarchy. In another way, due to the "optimal" Young's modulus in gecko's feet, the multilevel hierarchy can easily acquire by gecko. Eq. **8** [10] shows the lowest Young's modulus needed for different conditions (as shown in Fig. 4.11c).

$$E \geq \frac{8\gamma L^4}{3d^2t^3} \quad \cdots\cdots\cdots\cdots\cdots\cdots\cdots\cdots\cdots\cdots\cdots\cdots\cdots \quad (8)$$

Obviously, we can find out the Young's modulus needed for taper shape pillar is much lower than sheer pillar shape used in the most of synthetic gecko adhesives. The result revealed the taper shape can break the limitation of material characteristics (such as Young's modulus limitation) through successfully designed structure and shows an optimal model which enhanced the stability and lifetime within the high adhesion, for any kind of material.
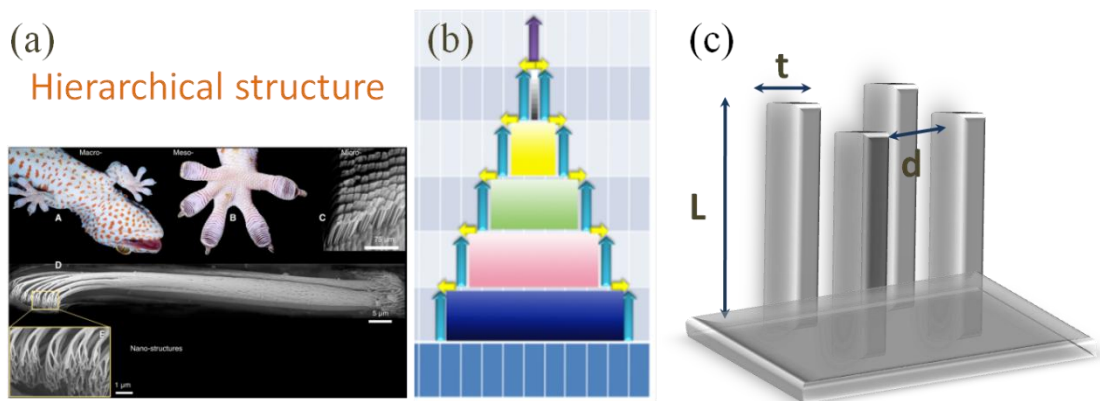
Figure 4.11 Illustrate hierarchy (a) of gecko and (b) of taper shape as a hierarchy-like by "cake" model. (c) Illustration of Eq. 8.

4.2.2 Unidirectional force through slanted angle

In addition to high AR and small radius of structures, a directional angle of nanostructure is another crucial factor for anisotropic, reversible dry adhesive. It is because an angled structure significantly lowers the effective modulus of the surface from Eq. **9** [9].

$$E_{eff} = \frac{3EID\sin\theta}{L^2\cos^2\theta[1\pm\mu\tan\theta]}$$ · (9)

where E is the elastic modulus, I is the moment of inertia ($I = \pi R^4/4$, R is the radius of hair), D is the hair density, L is the hair length, μ is the friction coefficient, and θ is the slanted angle. According to Dahlquist criterion we have mentioned previously, the effective modulus should be less than 100 kPa for ensuring a tacky surface. If the structures are slanted, the effective modulus can be greatly reduced without the need of structures with extremely high AR, which we mentioned in Chapter 2.3, including the risk of self-matting and structural buckling within the limited modulus of polymers. As shown in Fig. 4.12, for 80 nm nanohairs with AR of 15 ($E = 19.8$ MPa, $D = 6.3\times10^8$ cm^{-2}, $\mu = 0.25$), the effective modulus decreases less than 100 kPa when the structures are slanted with less than 73° angle with respect to the horizontal plane.

Another fascinating property of the slanted structures is a controllable adhesion by varying the applied shear force. Efficient climbing relies on this behavior. By contrast, materials such as pressure-sensitive adhesive tapes require a substantial preload to achieve adhesion and a similarly large force to achieve detachment. The attached and detached mechanism of our slanted taper is shown in Fig. 4.13.
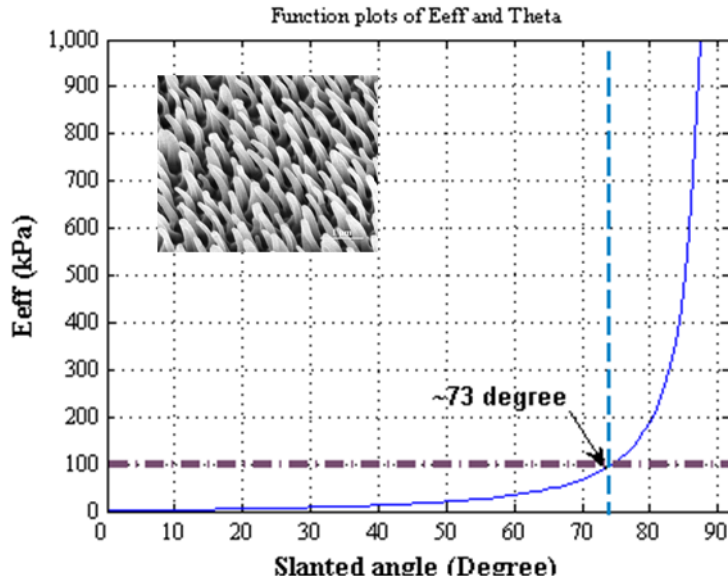
Figure 4.12 Displays the simulation of E_{eff} versus slanted angle. Clearly, the E_{eff} drop below 100 kPa, which fit the Dahlquist criterion, with decreasing slanted angle after 73°.
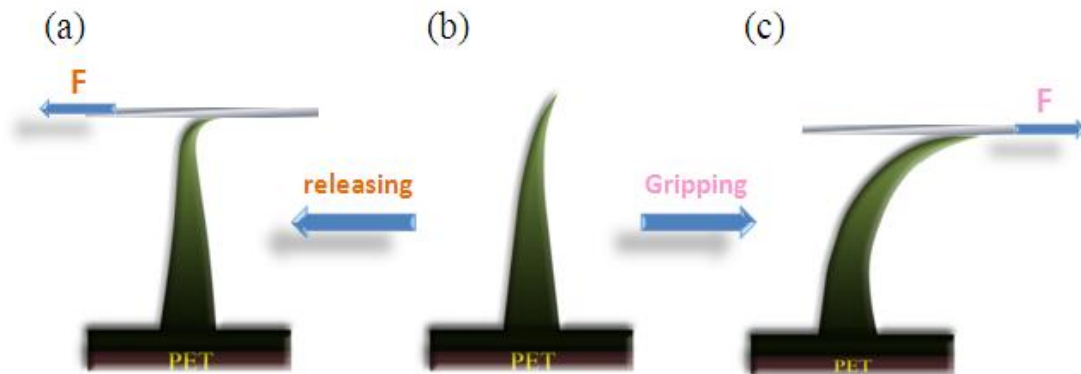
Figure 4.13 Theoretical analysis of directional adhesion mechanism of the slanted taper shaped pillars. An illustration showed the change of leaning angle of the slanted taper nanohairs when the adhesive is pulled in (a) the gripping, (b) initial state and (c) releasing direction.

We hypothesize that the observed anisotropic behavior arises primarily due to

the stresses caused by the moment created when the taper is sheared. This can be understood by analysis of the rotation of the tip during shear loading in each direction (Fig. 4.13). The original angle, φ, introduces a moment that is relative to the magnitude of the angle change from its undeformed state. The peeling moment is increased if the tapered pillar is sheared in the releasing direction because it increases the already present tip rotation to a larger angle ($φ_r$), increasing $Δφ$ as seen in Fig. 4.13c. This increased moment peels the leading edge, eventually detaching and overturning the fiber tip. However, when sheared in the gripping direction, the fiber tip begins to return to its original angle, reducing the moment to zero (Fig. 4.13a). When the magnitude of the moment is near zero, the normal stress distribution at the interface is more evenly distributed, reducing the chances of detachment. After this point, if the shearing in the gripping direction is continued, $Δφ$ changes and begins to increase in magnitude, eventually causing the leading edge (left) in detachment. The initial decrease in moment for shearing in the gripping direction increases the allowable displacement before detachment occurs, which means adhesion increased when shear force is applied in a preferred direction, in contrast to the releasing direction where the moment increases immediately. The increased displacement in the gripping direction allows the fibers to stretch and maintain contact, leading to high interfacial shear strength and anisotropy. All the shear and normal forces were recorded at the adhesive's failure point within our experiment. Taper shaped pillars we fabricated with slanted angle by pressure technique are shown in Fig. 4.14.

68
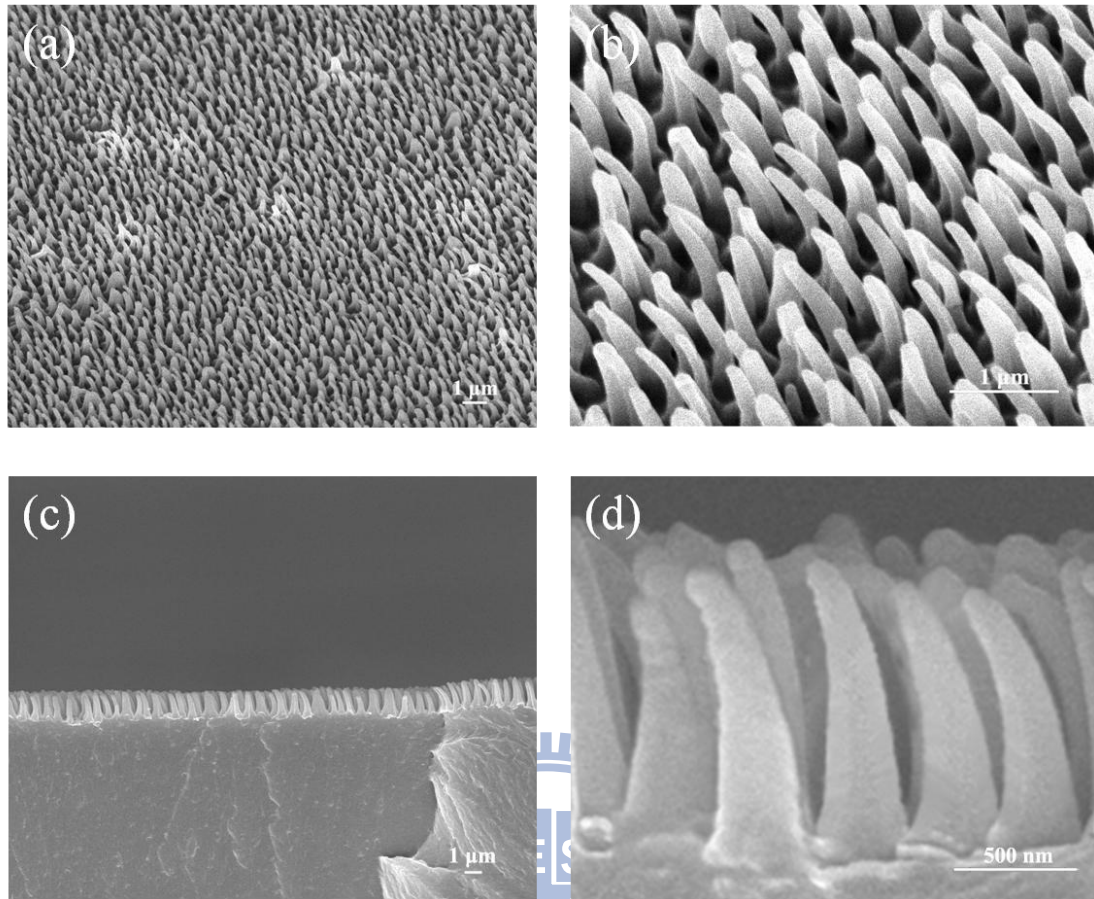
Figure 4.14 Taper shaped pillars with slanted angle we fabricated by pressure technique. (a) Low magnification. (b) High magnification of tilted SEM image of the structure. (c) Low magnification and (d) high magnification from cross-view.

The shear force was greatly reduced to 2.1 N/cm^2 when the sample was pulled in releasing direction, suggesting that the dry adhesive presented here can be used as a smart, directional adhesive patch with strong attachment (~21.5 N/cm^2) and easy detachment (~2.1 N/cm^2), with the hysteresis close to 13 as shown in Fig. 4.15. A simple peeling model can also explain the strong directional adhesion capability. According to the Kendall peeling model, the critical peel-off force (F_c) of a nanohair can be estimated with an assumption that the tip of slanted taper nanohairs forms intimate contact with the substrate as in an elastic tape, yielding [11-12]

$$P_{cr} = \frac{2\gamma b}{\sqrt{(1-\cos\theta)^2 + \frac{2\gamma}{Et} + 1 - \cos\theta}} \quad \ldots\ldots\ldots\ldots\ldots\ldots\ldots\ldots\ldots \quad (10)$$

where $\gamma = 100$ mJ/m^2 is the adhesive energy, θ is the peel-off angle, and $b = 50$ nm, $t = 100$ nm and $E = 19.8$ MPa are the width, thickness, and elastic modulus of the tape, respectively. Thus, the peel-off force can be expressed as a function of peeling angle for given parameters and the total peel-off force per unit area can be expressed by

$$P_{cr}(total) = \frac{2\gamma b}{\sqrt{(1-\cos\theta)^2 + \frac{2\gamma}{Et} + 1 - \cos\theta}} \bullet D \quad \ldots\ldots\ldots\ldots\ldots\ldots\ldots \quad (11)$$

where $D = 6.46*10^8$ cm^{-2} represented the hair density. Fig. 4.15 presented the peel-off force per unit area with varying peeling angles. As shown in Fig. 4.15, the peel-off force increased gradually with a stronger shear adhesion force. When the adhesive was pulled in the reverse direction, however, the leaning angle of nanohairs is increased from its initial value of 60° to 180°, and thus the peel-off force is greatly reduced. According to Eq. **11**, the peel-off forces are 21.5, 3.4, and 2.1 N/cm^2 for 0°, 90°, and 180°, respectively. The value of simulation is not quite fit with experimental data at a glance; however, the maximum value of simulation takes place at the angle around 0° which is scarcely possible on average day. Hence if the slanted angle was extended to 54°, the adhesion force will be around 8 N/cm^2 which agrees fairly well with our experimental results (maximum shear adhesion of ~8 N/cm^2 in the forward direction and ~1.4 N/cm^2 in the reverse direction as shown in Fig. 4.16).The diagram in Fig. 4.17 gave us a comparison between taper shape and pillar shape, then we can find out the higher adhesion of taper shape than pillars'. There is still remaining a large space we can improve between 8 N/cm^2 to 21.5 N/cm^2 from Fig 4.15. The

possible reason which restricts the extension of slanted angle may be the way to measure is not efficient enough.
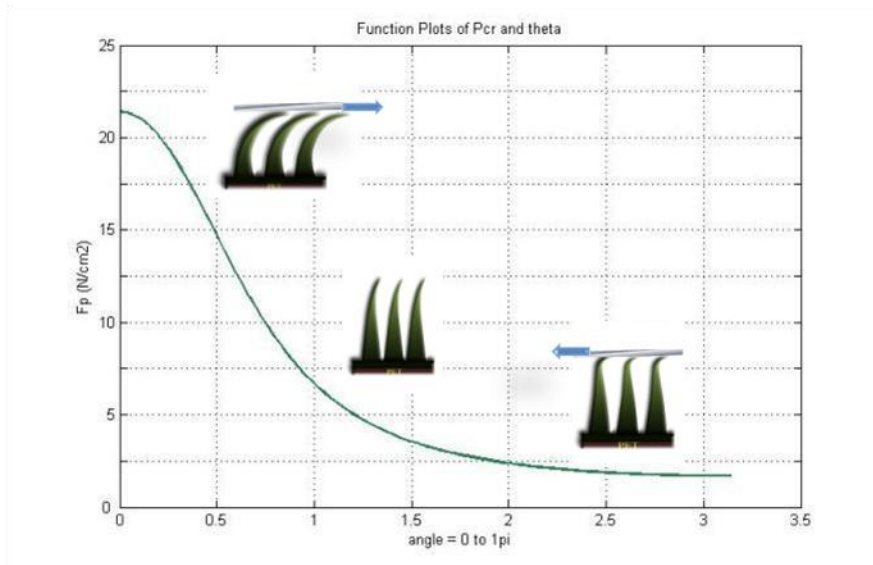
Figure 4.15 Simulation of critical peeling-off forces as a function of peeling angle.
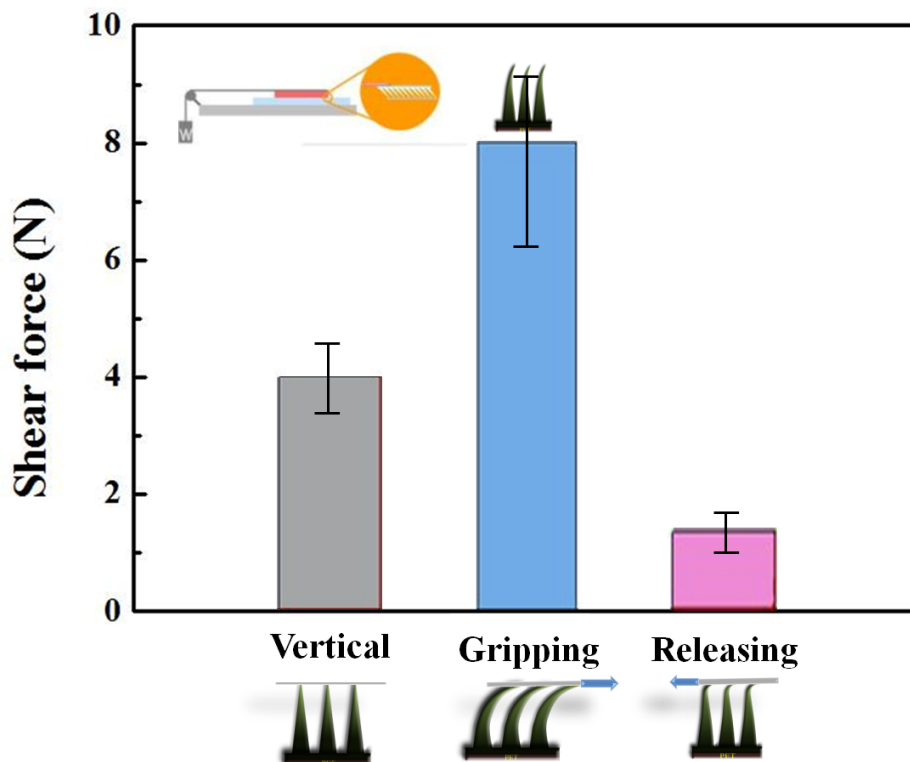
Figure 4.16 Measurement of shear force for various cases with an adhesive patch of

1.0 cm^2. The taper nanohairs were composed of soft PUA.
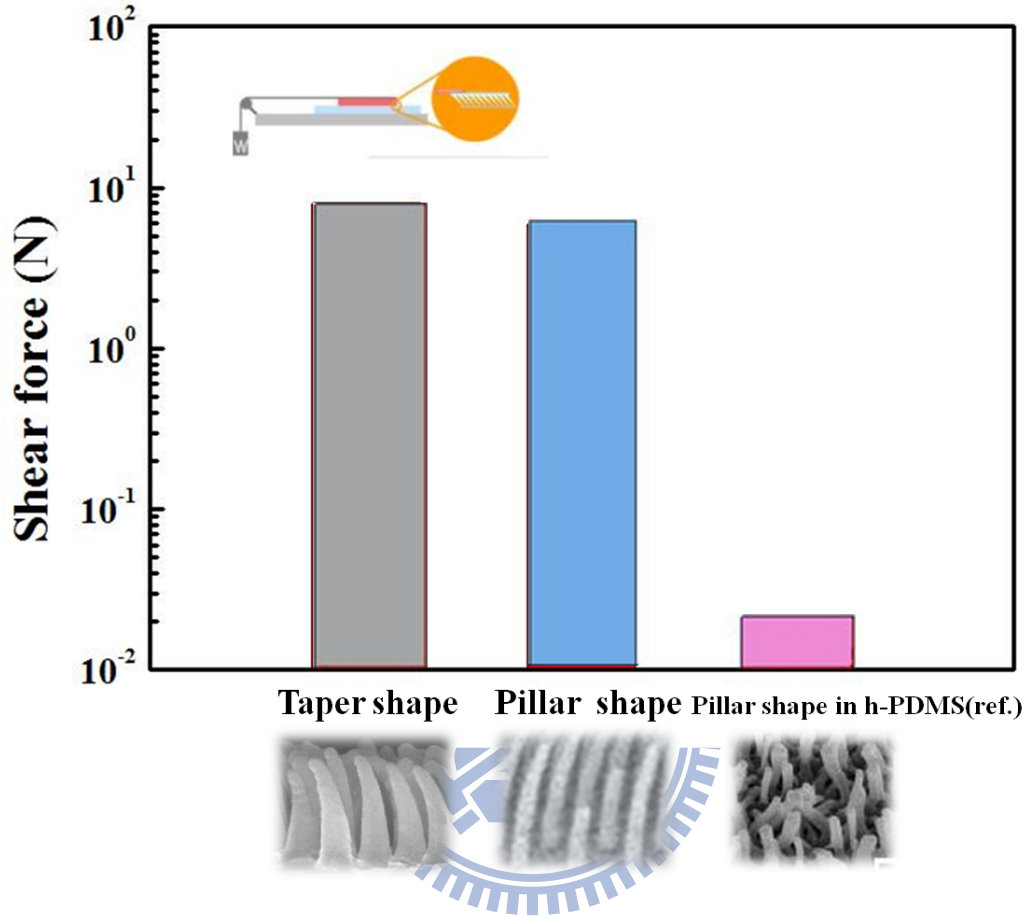
Figure 4.17 Giving a comparison between taper shape and pillar [5] shape, we can find out the higher adhesion of taper shape than pillars' can account for the higher density, longer length or adhere efficiently we discuss previously.

Taking the density and H$_{max}$ parameter into Eq. **11** (Eq. **12**) to show how the Young's modulus work in the motion, we can find out Young's modulus with a few effects on P$_{cr}$ in the same condition of length and density as shown in Fig. 4.18. That is, taper pillar is such a great solution, which isn't from material but structure, for polymer-based adhesives.

$$P_{cr}(total) = \frac{2 \cdot 10^{14} R^2 \cdot \gamma \cdot b \cdot \varphi_{max}}{\left(\sqrt{(1-\cos\theta)^2 + \frac{2\gamma}{Et}} + 1 - \cos\theta\right)(W+R)^2} \quad \dots\dots\dots\dots\dots \quad (12)$$

where the φ_{max} stands for the maximum area fraction of a given hair pattern. It can be shown that $\varphi_{max} = \pi/2\sqrt{3}$ for a triangular lattice (Fig 4.10a).
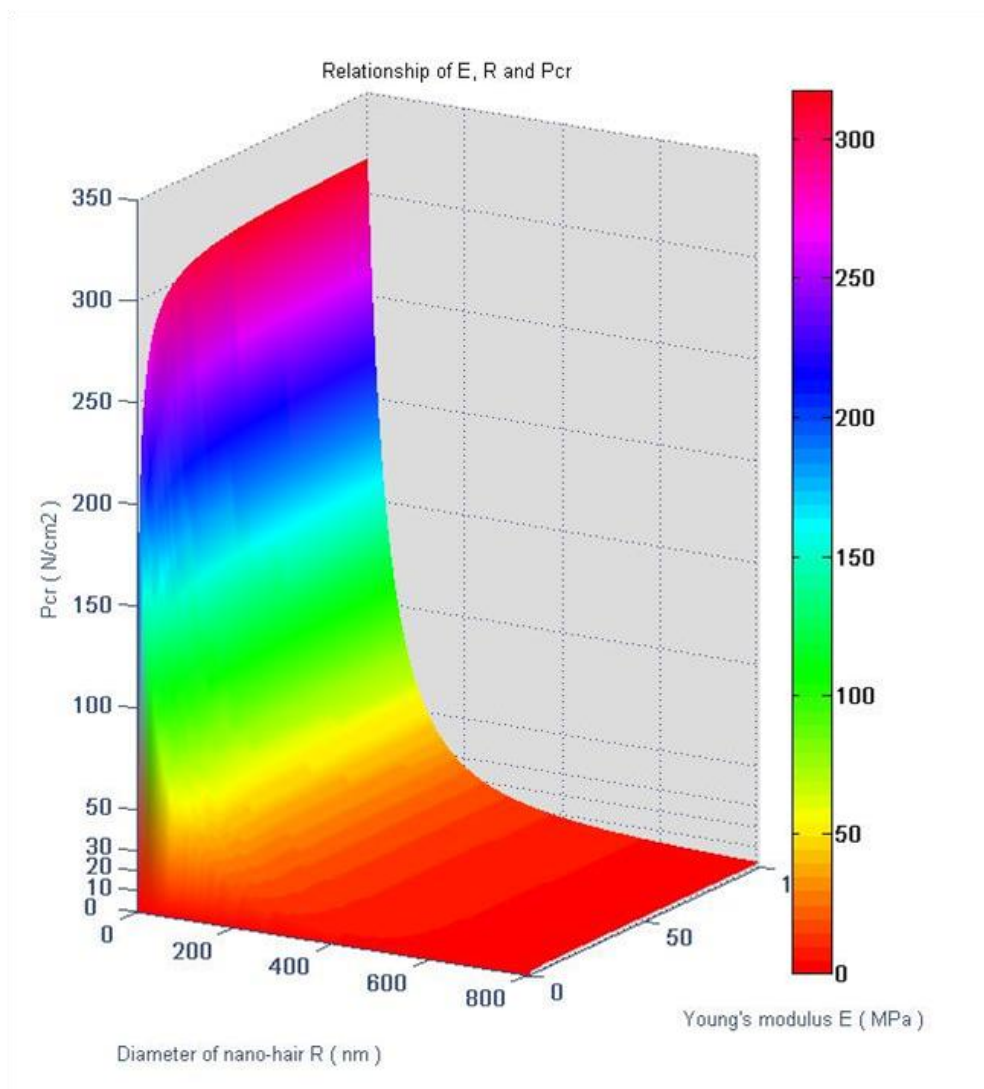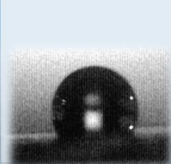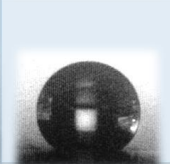
Figure 4.18 The relationship between P_{cr}, diameter and Young's modulus (E). The graph indicated t few effect from Young's modulus on P_{cr}, and smaller diameter is essential for larger adhesion.

4.2.3 Self-cleaning

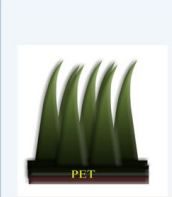Gecko with special self-cleaning via walking steps is well known for scientists. Self-cleaning ability will occur rapidly as a consequence of energetic disequilibrium; particles tend to remain attached to the wall rather than to the spatula. For dirt or particle in daily life, equal energy is required to separate the particle from the wall and from the spatula. Unless particles are very small, many spatulas must be attached simultaneously to a single particle to balance the interaction energy between a spherical dirt particle and a planar wall (W_{pw}). There are more details and theories we had mentioned in section 2.3.2. Applying the same assumption from gecko to our taper shape structure, we may conclude the dirt will transfer to wall due to the difference between W_{pw} and W_{pt} (the interaction energy between a spherical dirt particle and taper pillar). Approaching this feature, an optimal density is required. It avoids particles for dropping down to the space between pillars but still keep the balance between W_{pw} and W_{pt}, and stability which can suffer several times of steps. Both optimal density and reliable stability could be reached by our taper structure. To get this goal, the super-hydrophobicity as the gecko's setal arrays composed of an array of β-keratin pillars is considerable with a water contact angle of 160° and with a contact angle of 93° on flat β-keratin surface but setal arrays from gecko. The water contact angle is usually used to measure self-cleaning ability. Getting the same results from our taper shaped structure, we observe the contact angle is increasing from 72° (hydrophilic) to 148° (hydrophobic) (Table 3). This is deserved to mention that this level of hydrophobisity is enough for daily using. From Table 3, taper shape clearly showed the advantage of self-cleaning ability over pillar shape. Explanations and reasons are as follows. Generally, high contact angle is induced by nanostructure and low sliding angle caused by nano- and microstructures such as lotus as shown in Fig. 4.19a. Lotus is on behalf of super hydrophobic surfaces in Cassie's state, and exhibit a

high CA and very low CA hysteresis, in another way, owning to its high adhesive (high CA hysteresis) properties, gecko is the representative of the high CA which is referred to contact area. From Fig. 4.19b, we can deduce the nano-slanted taper shape from offering enough contact area for adhesion, while the contact area of microstructure or vertical structure is insufficient for high adhesion. Air trapping via nano- or micro-structure is critical for high CA; accordingly, efficiently trapped air is much more important than other factors. Both taper and pillar types are initially in Cassie's state and contribute very large fraction of air on the surface. Yet the air pockets of pillar type is in a flow tending condition, which is risky of transferring to Wenzel's state because it's continuous interface with outside air from top to bottom. As to taper type, sealed pockets tending condition will lead to flow unfriendly at bottom which is illustrated in Fig. 4.19b-c.

65°	94°	100°	125°	148°	148°
Scarcely air pocket, flat surface of PUA	A few air pocket, pillar shape of PUA	Few air pocket due to shorter taper shape of PUA	With larger air pocket, longer taper shape of PUA	Largest air pocket induced after fluroalkylsilane coating	Dual features of high CA and hysteresis angle show the water cleaning potential

Table 4.3 Measurement of contact angle for various cases with a dry adhesive pad.
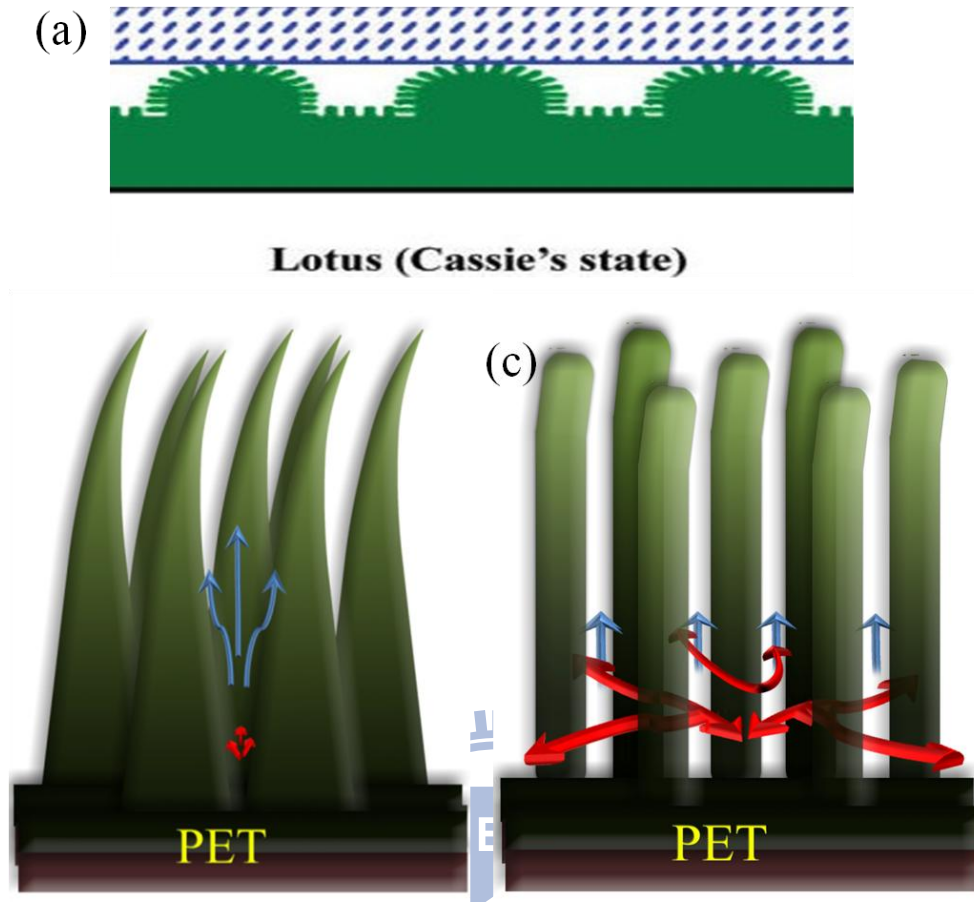
Figure 4.19 Schematic mechanism of high CA. (a) High contact angle is induced by nanostructure and low sliding angle caused by nano- and microstructures. (b,c) Illustration of the self-cleaning properties from gecko to taper shape and pillar shape adhesives. It is clearly displaying the air flowing direction which we concerned as the main reason to bring about hydrophobicity.

4.2.4 Demonstration and application

As a demonstration of the adhesion of the taper nanohair arrays, a small area of 1 cm^2 was evaluated through a frictional adhesion test as shown in Fig. 4.20b. Fig. 4.20a presented the mold and the tape of PUA after replicating.As to the measurement, a flexible adhesives with slanted nano-taper pillars attached to a glass slide that supported a counter weight in gripping direction (Fig. 4.20b) under a preload of 0.5 N

cm^{-2}. During the shear-adhesion test, no external normal load was applied. To verify the contamination, Fig 4.20c presented the adhesive after detaching from glass and the water droplet with high CA, which implied the water cleaning ability, on the adhesive, respectively.
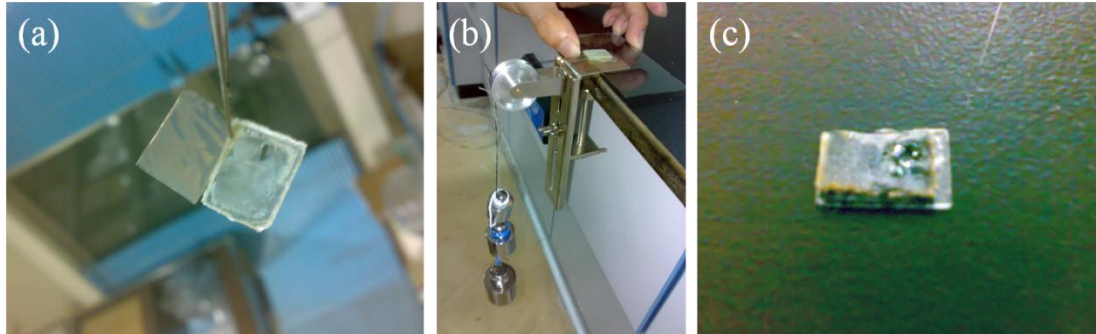
Figure 4.20 Photographs of (a) tape of PUA after replicating and the mold. (b) counter weitht measured system. (c) the high CA of tape after detaching from the glass.
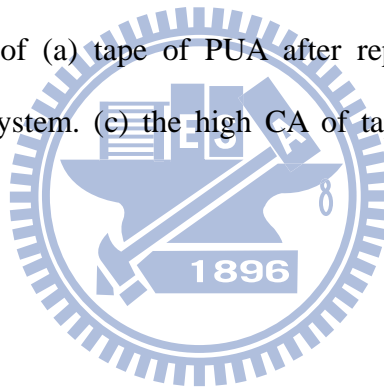
Chapter 5: Conclusion

We successfully presented an approach to fabricate angled taper nanohair arrays as an excellent directional, reusable and water cleanable gecko-mimicking dry adhesive in large area. From Dahlquist's criterion, an ideal taper nanohair of PUA that consist a length of 1.3 μm and a diameter of 380 nm was designed. By using taper AAO mold via decoupling two-step HA process reported firstly by us, taper nanohairs with slanted angle were fabricated. The angled taper nanohair did facilitate the stability and self-cleaning properties compared with pillar nanohairs while still maintain a great directional adhesion. Moreover, remarkably directional force exhibited by angled taper nanohair arrays is showing here with strong shear attachment (~8 N/cm^2) in the gripping direction and easy releasing(~1.4 N/cm^2) in the reverse direction (pulled against the angled direction of hairs). The smart adhesive presented here would enable the climbing robots, cleaning transport system such as LCD factory and non-residue sticker for future generation. A further study should be done on longer length or stiffer material to improve the adhesion capability against rough surfaces outside the laboratory.

Reference

Chapter 1

[1]   J. E. Gordon, *UK: Pelican–Penguin.***1976**

[2]   S. Eustis, M. A. El-Sayed, *Chem. Soc. Rev.* **2006**, 35, 209.

[3]   L. Gao, T. J. McCarthy, *J. Am. Chem. Soc.* **2006**, 128, 9052.

[4]   B. Bhushan, , Y. C. Jung, K. Koch, *Phil. Trans. R. Soc. A* **1986**, 367.

[5]   P. Vukusic, J. R. Sambles, *Nature* **2003**, 424, 852.

[6]   D. G. Stavenga, S. Foletti, G. Palasantzas, K. Arikawa, *Proc. R. Soc. B* **2006**, 273, 661.

[7]   P. B. Clapham, M. C. Hutley, *Nature* **1973**, 244, 281.

[8]   X. Gao, X. Yan, X. Yao, L. Xu, K. Zhang, J. Zhang, B. Yang, L. Jiang,. *Adv. Mater.* **2007** 19, 2213.

[9]   K. Autumn, Y. A. Liang, T. S. Hsieh, W. Zesch, W. P. Chan, T. W. Kenny, R. Fearing, R. J. Full, *Nature* **2000**, 405, 681.

[10] Y. Tian, N. Pesika, H. Zeng, K. Rosenberg, B. Zhao, P. McGuiggan, K. Autumn, J. Israelachvili, *Proc. Natl. Acad. Sci. U.S.A.* **2006**, 103, 19320.

[11] Sarikaya, M.; Tamerler, C.; Jen, A. K. Y.; Schulten, K.; Baneyx, F. *Nat. Mater.* **2003**, *2*, 577-585.

[12] W. R. Hansen, K. Autumn, *Proc. Natl. Acad. Sci. U.S.A.* **2005**, 102, 385.

Chapter 2

[1] F. Keller, M. S. Hunter, D. L. Robinson, *J. Electrochem. Soc.* **1953**, 100, 411.

[2] M. S. Hunter, P. Fowle, *J. Electrochem. Soc.* **1954**, 101, 481.

[3] G. E. Thompson, G. C. Wood, *Nature* **1981**, 290, 230.

[4] M. M. Lohrengel, *Mater. Sci. Eng. R* **1993**, 11, 243.

[5] J. W. Diggle, T. C. Downie, C.W. Goulding, *Chem. Rev.* **1969**, 69, 365.

[6] G. E. Thompson, R. C. Furneaux, G. C. Wood, J. A. Richardson, J. S. Goode, *Nature* **1978**, 272, 433.

[7] G. C. Wood, J. P. O'Sullivan, *Electrochim. Acta* **1970**, 15, 1865.

[8] A. P. Li, F. Muller, Birner, A. K. Nielsch, U. Gösele, *J. Appl. Phys.* **1998**, 84, 6023.

[9] E. H. Jerrod, R. H. Kurt, *Nat. Mater.* **2009**, 8, 415.

[10] C. R. Martin, *Science* **1994,** 266, 1961.

[11] S. R. Nicewarner-Pena, *Science* **2001** 249, 137.

[12] S. B. Lee, et al. *Science* **2002,** 296, 2198.

[13] H. Masuda, F. Hasegwa, S. Ono, *J. Electrochem. Soc.* **1997**, 144, L127.

[14] H. Masuda, K. Fukuda, *Science* **1995**, 268, 1466.

[15] F. Li, L. Zhang, R. M. Metzger, *Chem. Mater.* **1998**, 10, 2470.

[16] S. Shingubara, K. Morimoto, H. Sakaue, T. Takahagi, *Electrochem. Solid-State Lett.* **2004**, 7, E15.

[17] K. Nielsch, J. Choi, K. Schwirn, R. B.Wehrspohn, U. Gosele, *Nano Lett.* **2002**, *2*, 677.

[18] W. Lee, R. Ji, U. Go¨sele, K. Nielsch, *Nat. Mater.* **2006**, 5, 741.

[19] K. Ebihara, H. Takahashi, M. Nagayama, *J. Met. Finish. Soc. Jpn,* **1983**. 34, 548.

[20] P. Csokan, C. Chen, *Electroplat. Metal Finishing* **1962,** 15, 75.

[21] E. Lichtenberger, A. Domony, P. Csokan, *Mechanics of Materials* **1960,** 11, 701.

[22] L. Yanbo, Z. Maojun, M. Li, S. Wenzhong, *Nanotechnology* **2006**, 17, 5101.

[23] L.Woo, S. Kathrin, S. Martin, P. Eckard, S. Roland, G. S. Ulrich, *Nat. Mater.* **2008**, 3, 234.

[24] V. P. Parkhutik, V. I. Shershulsky, *J. Phys. D: Appl. Phys.* **1992**, 25, 1258.

[25] J. Siejka, C. Ortega, *J. Electrochem. Soc.* **1997**, 124, 883.

[26] O. Jessensky, F. Muller, U. Gösele, *Appl. Phys. Lett.* **1998**, 72, 1173.

[27] S. Z. Chu, K. Wada, S. Inoue, M. Isogai, A. Yasumori, *Adv. Mater.* **2005**, 17, 2115.

[28] T. Yanagishita, K. Yasui, T. Kondo, Y. Kawamoto, K. Nishio, H. Masuda, *Chemistry Letters* **2007**, 36, 530.

[29] E. Delamarche, H. Schmid, B. Michel, H. Biebuyck, *Adv. Mater.* **1997**, 17. 741.

[30] P. Yoo, S. J. Choi, J. H. Kim, D. Suh, S. J. Baek, T. W. Kim, H. H. Lee, *Chem. Mater.* **2004,** 16, 5000.

[31] Y. K. Dahl, K. Hyewon, K. Tae, H. L. Hong, *Nano Lett.* **2004**, 4, 633.

[32] C. V. G. Reddy, S. V. Manorama, V. J. Rao, A. Lobo, S. K. Kulkarni, *Thin Solid Films* **1999**, 1-2, 261.

[33] T. W. Odom, J. C. Love, D. B. Wolfe, K. E. Paul, G. M. Whitesides, *Langmuir* **2002,** 18, 5314.

[34] C. T. Wu, F. H. Ko, *Appl. Phys. Lett.* 2007, 90, 191901.

[35] S. J. Choi, P. J. Yoo, S. J. Baek, T. W. Kim, H. H. Lee, *J. Am. Chem. Soc.* **2004**, 126, 7744.

[36] H. Schmid, B. Michel, *Macromolecules* **2000**, 33, 3042.

[37] K. M. Choi, J. A. Rogers, *J. Am. Chem. Soc.* **2003**, 125, 4060.

[38] K. Autumn, Y. A. Liang, T. S. Hsieh, W. Zesch, W. P. Chan, T. W. Kenny, R. Fearing, R. J. Full, *Nature* **2000**, 405, 681.

[39] H. Gao, X. Wang, H. Yao, S. Gorb, E. Arzt, *Mechanics of Materials* **2005,** 37,

275.

[40] K. Autumn, M. Sitti, Y. A. Liang, A. M. Peattie, W. R. Hansen, S. Sponberg, T. W. Kenny, R. Fearing, J. N. Israelachvili, R. J. Full, *Proc. Natl. Acad. Sci.* **2002**, 99, 12252.

[41] W. R. Hansen, K. Autumn, *Proc. Natl. Acad. Sci. U.S.A.* **2005**, 102, 385.

[42] M. Sitti, R.S. Fearing, *Adhes. Sci. Technol.* **2003,** 17, 1055.

[43] C. Greiner, A. Campo, E. Arzt, *Langmuir* **2007,** 23, 3495.

[44] A. K. Geim, S. V. Dubonos, I. V. Grigorieva, K.S. Novoselov, A. A. Zhukov, S. Y. Shapoval, *Nat. Mater.* **2003,** 2, 461.

[45] H. E. Jeong, S. H. Lee, P. Kim, K. Y. Suh, *Nano Lett.* **2006,** 6, 1508.

[46] C. Majidi, R. E. Groff, Y. Maeno, B. Schubert, S. Baek, B. Bush, R. Maboudian, N. Gravish, M. Wilkinson, K. Autumn, R. S. Fearing, *Phys. Rev. Lett.* **2006,** 97.

[47] T. Kim, H. E. Jeong, K. Y. Suh, H. H. Lee, *Adv. Mater.* **2009,** 21, 2276.

[48] L. Ge, S. Sethi, L. Ci, P. M. Ajayan, A. Dhinojwala, *Proc. Natl. Acad. Sci. U.S.A.* **2007,** 104, 10792.

[49] L. T. Qu, L. M. Dai, M. Stone, Z. H. Xia, Z. L. Wang, *Science* **2008,** 322, 238.

[50] S. Kim, M. Spenko, S. Trujillo, B. Heyneman, D. Santos, M. R. Cutkosky, *IEEE Trans. Robotics* **2008,** 24, 65.

[51] A. Mahdavi, L. Ferreira, C. Sundback, J. W. Nichol, E. P. Chan, D. J. D. Carter, C. J. Bettinger, S. Patanavanich, L. Chignozha, E. Ben-Joseph, A. Galakatos, H. Pryor, I. Pomerantseva, P. T. Masiakos, W. Faquin, A. Zumbuehl, S. Hong, J. Borenstein, J. Vacanti, R. Langer, J. M. Karp, *Proc. Natl. Acad. Sci..* **2008,** 105, 2307.

[52] D. S. Kim, H. S. Lee, J. Lee, S. Kim, K. H. Lee, W. Moon, T. H. Kwon, *Microsys. Technol.* **2007**, 13, 601.

[53] C. Greiner, E. Arzt, A. del Campo, *Adv. Mater.* **2009**, 21, 479.

[54] M. P. Murphy, B. Aksak, M. Sitti, *Small* **2009**, 5, 170.

[55] B. Yurdumakan, N. R. Raravikar, P. M. Ajayan, A. Dhinojwala, *Chem. Commun.* **2005**, 3799.

[56] L. F. Boesel, C. Greiner, E. Arzt, A. del Campo, *Adv. Mater.* **2010**, 22, 1.

[57] S. Kim, M. Sitti, C. Y. Hui, R. Long, A. Jagota, *Appl. Phys. Lett.* **2007**, 91.

[58] A. del Campo, C. Greiner, J. *Micromech. Microeng.* **2007**, 17, R81.

[59] M. P. Murphy, S. Kim, M. Sitti, *Appl. Mater. Interfaces* **2009**, 1, 849.

[60] A. Jagota, S. J. Bennison, *Integr. Comp. Biol.* **2002**, 42, 1140.

[61] B. Aksak, M. P. Murphy, M. Sitti, *Langmuir* **2007**, 23, 3322.

[62] J. Lee, R. S. Fearing, K. Komvopoulos, *Appl. Phys. Lett.* **2008**, 93, 191910.

[63] L. Qu, L. Dai, *Adv. Mater.* **2007**, 19, 3844.

[64] C. T. Wirth, S. Hofmann, J. Robertson, *Diamond Relat. Mater.* **2008**, 17, 1518.

[65] Y. Zhao, T. Tong, L. Delzeit, A. Kashani, M. Meyyappan, A. Majumdar, *J. Vac. Sci. Technol. B* **2006**, 24, 331.

[66] R. N. Wenzel, *Ind. Eng. Chem.* **1936**, 28, 988.

[67] D. Ö ner, T. J. McCarthy, *Langmuir* **2000**, 16, 7777.

[68] A. Lafuma, D. Quere, *Nat. Mater.* **2003**, 2, 457.

[69] W. Barthlott, C. Neinhuis, *Planta* **1997**, 202, 1.

[70] C. Neinhuis, *Ann. Bot.* **1997**, 79, 667.

[71] K. L. Johnson, K. Kendall, A. D. Roberts, *Proc. R. Soc. A* **1971**, 324, 301.

[72] E. Arzt, S. Gorb, R. Spolenak, *Proc. Natl. Acad. Sci.* **2003**, 100, 10603.

[73] K. Autumm, A. Dittmore, D. Santos, M. Spenko, M. Cutkosky, *J. Exp. Biol.* **2006**, 206, 3569.

[74] B. X. Zhao, N. Pesika, H. B. Zeng, Z. S. Wei, Y. F. Chen, K. Autumn, K. Turner, J. Israelachvili, *J. Phys. Chem. B* **2009**, 113, 3615.

[75] K. Autumn, C. Majidi, R.E. Groff, A. Dittmore, R. Fearing, *J. Exp. Biol.* **2006**,
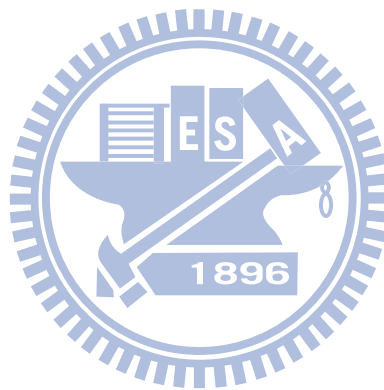
209, 3558.

[76] N. J. Glassmaker, A. Jagota, C. Y. Hui, J. Kim, *J. R. Soc. Interface* **2004**, 1, 23.

[77] C. Y. Hui, A. Jagota, Y. Y. Lin, E. J. Kramer, *Langmuir* **2002**, 18, 1394.

[78] H. Yao, H. Gao, *J. Mech. Phys. Solids* **2006**, 54, 1120.

[79] H. J. Gao, H. M. Yao, *Proc. Natl. Acad. Sci.* **2004**, 101, 7851.

Chapter 4

[1] W. Lee, R. Ji, U. Gosele, K. Nielsch, *Nat. Mater.* **2006**, 5, 741.

[2] K. Autumn, Y. A. Liang, T. S. Hsieh, W. Zesch, W. P. Chan, T. W. Kenny, R. Fearing, R. J. Full, *Nature* **2000**, 405, 681.

[3] T. Kim, H. E. Jeong, K. Y. Suh, H. H. Lee, *Adv. Mater.* **2009,** 21, 2276.

[4] J. Lee, R. S. Fearing, K. Komvopoulos, *Appl. Phys. Lett.* **2008**, 93, 191910.

[5] W. K. Cho, I. S. Choi, *Adv. Funct. Mater.* **2008**, 18, 1089.

[6] C. Greiner, E. Arzt, A. del Campo, *Adv. Mater.* **2009**, 21, 479.

[7] M. P. Murphy, B. Aksak, M. Sitti, *Small* **2009**, 5, 170.

[8] K. Autumn, C. Majidi, R. E. Groff, A. Dittmore, R. Fearing, *J. Exp. Biol.* **2006**, 209, 3558.

[9] N. J. Glassmaker, A. Jagota, C. Y. Hui, J. Kim, *J. R. Soc. Interface* **2004**, 1, 23.

[10] C. Y. Hui, A. Jagota, Y. Y. Lin, E. J. Kramer, *Langmuir* **2002**, 18, 1394.

[11] H. Yao, H. Gao, *J. Mech. Phys. Solids* **2006**, 54, 1120.

[12] H. J. Gao, H. M. Yao, *Proc. Natl. Acad. Sci.* **2004**, 101, 7851.